DOKUZ EYLÜL UNIVERSITY
GRADUATE SCHOOL OF NATURAL AND APPLIED SCIENCES

NUMERICAL ANALYSIS OF EJECTOR IN A COOLING SYSTEM

by
Okan GÖK

August, 2020
İZMİR

NUMERICAL ANALYSIS OF EJECTOR IN A COOLING SYSTEM

A Thesis Submitted to the
Graduate School of Natural and Applied Sciences of Dokuz Eylül University
In Partial Fulfillment of the Requirements for the Degree of Master of Science
in Mechanical Engineering, Thermodynamics Program

by
Okan GÖK

August, 2020
İZMİR

M.Sc THESIS EXAMINATION RESULT FORM

We have read the thesis entitled "**NUMERICAL ANALYSIS OF EJECTOR IN A COOLING SYSTEM**" completed by **OKAN GÖK** under supervision of **PROF.DR. AYTUNÇ EREK** and we certify that in our opinion it is fully adequate, in scope and in quality, as a thesis for the degree of Master of Science.

………………………………………….

Prof. Dr. Aytunç EREK

Supervisor

………………………………

Assoc.Prof.Dr. Mehmet Akif EZAN

(Jury Member)

…………………………………

Assoc.Prof.Dr. Erdal ÇETKİN

(Jury Member)

Prof. Dr. Özgür ÖZÇELİK

Director

Graduate School of Natural and Applied Sciences

ACKNOWLEDGEMENT

Before all the sentences to be said, I present my sincere gratitude to my advisor Prof. Dr. Aytunç EREK, for the patient guidance, encouragement, and useful criticism from the beginning of this research. I am proud to work with him as a student because he teaches me to gain a different perspective on engineering and research.

Secondly, I would like to thank Dr. Ayşe Uğurcan ATMACA, who shared her support, experience, and suggestions with me in the evaluation of the research. I am very grateful for the way she has guided me with all his sincere ideas.

Besides, I would like to acknowledge the support of the Scientific and Technological Research Council of Turkey (TÜBİTAK) and entitled “Design improvement and numerical and experimental performance investigation of the ejectors used in the vapor compression refrigeration cycle” under grant number of 116M367.

I also express my gratitude to Saime ÖZDEMİR, who has a great place in my life and supports me in every respect. Most importantly, I am grateful to them for the endless patience, support, and perseverance of my entire family, especially my mother and father.

Okan GÖK

NUMERICAL ANALYSIS OF EJECTOR IN A COOLING SYSTEM

ABSTRACT

Nowadays, environmentally-friendly solutions are being investigated instead of using fossil fuel and electrical energy systems, depending on the increasing energy consumption. Therefore, many studies have been carried out on a heat-driven ejector refrigeration cycle using waste heat or renewable energy sources as an alternative to the conventional refrigeration cycle. In this thesis study, the performance of different refrigerants for two geometric parameters was evaluated under the selected operating condition in numerical modeling of the ejector used in the heat-driven ejector refrigeration cycle. In numerical analyses, R1234yf, and R1234ze(E) having low Global Warming Potential value from Hydrofluoroolefin, and R1234a which will be excluded due to the high Global Warming Potential value were used as the refrigerant. Computational Fluid Dynamics method is used for numerical modeling of the ejector by using ANSYS Fluent, a commercial software. In addition, the thermophysical properties of refrigerants were obtained using REFPROP v9.1 database. Entrainment ratio, one of the most important performance criteria for the ejector, was determined by Computational Fluid Dynamics analysis using the ejector geometry selected as a reference from the literature. In addition to the entrainment ratio, the flow structures were discussed in detail using axial Mach Number distributions, Mach Number contours, and shadowgraphs in the mixing section of the ejector. In this way, it will contribute to previous numerical modeling studies in the literature and guide future studies for more realistic performance improvement values.

Keywords: Heat-driven ejector refrigeration cycle, vapor-jet ejector, hidrofloroolefin (HFO) refrigerants, computational fluid dynamics (CFD), primary nozzle exit position, converging duct angle, entrainment ratio, shadowgraph

BİR SOĞUTMA SİSTEMİNDEKİ EJEKTÖRÜN SAYISAL ANALİZİ

ÖZ

Günümüzde artan enerji tüketimine bağlı olarak fosil yakıt ve elektrik enerjisi sistemleri kullanmak yerine çevre dostu çözümler araştırılmaktadır. Bu nedenle, geleneksel soğutma sistemlerine alternatif olarak atık ısı veya yenilenebilir enerji kaynakları kullanılarak harici ısı kaynaklı bir ejektör soğutma çevrimi üzerinde birçok çalışma yapılmaktadır. Bu tez çalışmasında, harici ısı kaynaklı ejektör soğutma çevriminde kullanılan ejektörün sayısal modellemesinde iki farklı geometrik parametre için farklı soğutucu akışkanların performansı, seçilen çalışma koşulları altında değerlendirilmiştir. Sayısal çalışmalarda soğutucu akışkan olarak, kullanım dışı kalacak olan R1234a, Hidrofloroolefin grubundan ve düşük Küresel Isınma Potansiyeli değerine sahip R1234yf ve R1234ze(E) kullanılmıştır. Hesaplamalı Akışkanlar Dinamiği yöntemi, ticari bir yazılım olan ANSYS Fluent program kullanılarak ejektörün sayısal modellemesi için kullanılmıştır. Soğutucu akışkanların termofiziksel özellikleri REFPROP v9.1 kullanılarak elde edilmiştir. Kullanılan soğutucu akışkana bağlı olarak, ejektörün her bir girişindeki kütlesel debileri ve ejektörün önemli bir performans kriteri olan kütlesel debiler oranı seçilen çalışma koşulları altında elde edilmiştir. Literatürden referans olarak seçilen ejektör geometrisi kullanılarak Hesaplamalı Akışkanlar Dinamiği analizleri aracılığıyla belirlenmiştir. Kütlesel debiler oranına ek olarak, ejektörün karışım bölümündeki akış yapıları, eksenel Mach Sayısı dağılımları, Mach Sayısı kontur grafikleri ve gölge grafiği kullanılarak detaylandırılmıştır. Elde edilen sonuçların değerlendirilmesiyle, literatürde daha önce yapılmış olan sayısal modelleme çalışmalarına katkıda bulunulması ve gelecekteki çalışmalarda daha gerçekçi performans iyileştirme değerlerinin elde edilmesine yön verilmesi amaçlanmaktadır.

Anahtar Kelimeler: Harici ısı kaynaklı ejektörlü soğutma çevrimi, buhar jet ejektörü, hidrofloroolefin (HFO) akışkanlar, hesaplamalı akışkanlar dinamiği (HAD), birinci lüle çıkış konumu, karışım bölümü daralma açısı, kütlesel debiler oranı, gölge grafiği

CONTENTS

LIST OF FIGURES

LIST OF TABLES

CHAPTER ONE
INTRODUCTION

Depending on the increasing energy requirement, both the environmental damage and the increasing depletion of energy resources pose a significant problem worldwide. In particular, the continuous and high-energy consumption of air conditioning, refrigerating, and freezing systems has a large share in the expenditure of energy resources. The main purpose of such systems is to reverse the direction of natural heat transfer using thermodynamic cycles to bring the temperature of the desired volume to the set temperature. Minimizing the energy consumed in the cooling effect intended for the places, components, and various devices in which refrigeration systems are used is a priority. The expansion valve used in the vapor-compression refrigeration cycle (VCRC) causes system-wide throttling losses. In this thesis, it was aimed to increase the performance of the refrigeration by adding an ejector to the vapor-compression refrigeration cycle. The content of the thesis consists of the numerical investigation of an ejector in the heat-driven ejector refrigeration cycle (HDERC) using different refrigerants in terms of different geometric parameters of the ejector. First of all, the background information about the ejector and heat-driven refrigeration cycle was given in this section. Secondly, the objectives and motivations of the thesis are presented, and then the methodology of the thesis was given. Finally, the general outlines of the thesis are summarized in this section.

1.1 Basics of the Ejector

Ejectors are used in many industrial applications ranging from many refrigeration and air conditioning applications to marine industries due to their easy assembly, simple structure, and low maintenance costs. This section provides a brief review of previous work on the basics of ejectors as well as their use in refrigeration and air-conditioning applications.

Ejectors are generally used to transfer, compress and mix gases, liquids, and solids that use gas or liquid as entraining. Ejectors can be compared to pumps with "no moving parts" in a simple analogy. The ejector is used to entrain the low-pressure secondary fluid and provide compression power by passing through the converging-diverging nozzle the high-pressure primary fluid that is driven by a pump. The ejector consists of basically four sections as follows; (i) primary converging-divergent nozzle, (ii) suction section (primary nozzle & secondary flow inlet) where primary and secondary fluid flows enter, respectively, (iii) mixing section and (iv) diffuser. The ejector flow diagram and the main parts that make up the ejector are presented schematically in Figure 1.1.

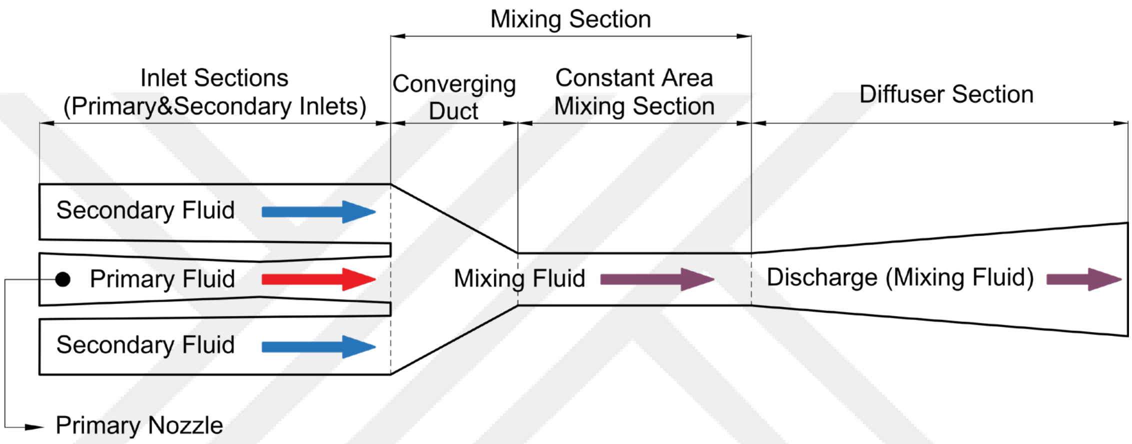

Figure 1.1 Flow diagram of primary and secondary fluids through the ejector and main parts of the ejector

The high-pressure primary fluid enters the ejector and expands to low pressure and high speed, usually supersonic condition, at the nozzle outlet through a converging-divergent nozzle. On the other hand, the secondary fluid, which has low pressure compared to the primary fluid, is entrained by the pressure difference at the primary nozzle outlet. The primary and secondary fluid are mixed at the inlet of the mixing section, where energy and momentum are transferred to the secondary fluid. At this point, primary and secondary fluids have the same pressure, which is called mixing pressure. In order to occur this transfer and flow between the primary and secondary fluids, the mixing pressure must be lower than the secondary fluid pressure. The complex flow structure that takes place in the mixing section of the ejector is examined in the literature with assumptions in different studies (Kornhauser, 1990; Li & Groll, 2005). In the mixing section of the ejector, the primary and secondary fluids are mixed, flowing in the form of a single flow stream, and shock series may occur. After that, the mixing pressure increases and passes through the diffuser at pressure value between the inlet pressures of the primary and secondary fluids. The single flow stream is lost its kinetic energy in the diffuser, thereby increasing the pressure. Hence the secondary fluid with low pressure is pressurized. In the next sections, numerical and experimental studies on the ejector in the literature are presented.

The entrainment ratio (w), the name given to the ratio of the secondary mass flow to the primary mass flow shown in Equation (1.1). The Entrainment ratio, one of the most important global performance parameters for ejector performance. As a general definition, the entrainment ratio (w) is defined as the measure of how much fluid mass can entrain or pump the ejector.

Compression ratio ($\prod_{comp}$) is another parameter in evaluating ejector performance, such as the entrainment ratio (w). The compression ratio is defined in Equation 1.2 as the ratio of the diffuser outlet pressure to the secondary inlet pressure. The outlet pressure of the ejector in the heat-driven ejector refrigeration cycle (HDERC) was determined by the condenser. The minimum pressure is equal to the vapor pressure at the temperature of the fluid at the ejector outlet. Similarly, the expansion ratio (ξ_{exp}) is also used. Expansion ratio (ξ_{exp}) is calculated as the ratio of primary nozzle inlet pressure to secondary fluid inlet pressure of the ejector, as shown in Equation 1.3.

$$w = \frac{\dot{m}_s}{\dot{m}_p} \tag{1.1}$$

$$\prod_{comp} = \frac{P_{diff,out}}{P_{s,in}} \tag{1.2}$$

$$\xi_{exp} = \frac{P_{p,in}}{P_{s,in}} \tag{1.3}$$

The parameters used to evaluate the ejector performance specified in Equation 1.1, Equation 1.2, and Equation 1.3 depend on the basic geometric dimensions and operating conditions of the ejector. In line with the numerical studies carried out in this thesis, flow structures in the ejector are presented, and the performance impact on global performance parameters is evaluated.

1.2 Historical Development and Types of the Ejector

The historical basis of the ejector concept dates back to the 1850s. Firstly, the patent study was made by Henri Giffard with the concept of injector, which is similar to the ejector in 1858 (Kranakis, 1982). Subsequently, the injector modified by Henri Giffard, where the mass flow of the primary fluid is controlled by needle, is shown in Figure 1.2 (Kranakis, 1982). The injector and ejector geometries are similar depending on the method of use in the application. The main difference between these two components is related to how the secondary fluid is driven. As the working principle of the ejector, the high energy primary fluid is passed through the primary nozzle, thereby suction by the secondary fluid. In the concept of injector, the primary and secondary fluids are pumped in order to provide transport and to mix at the rate determined by an external drive. The ejector, considered the first ejector to be produced, was produced by Charles Parsons around 1901 to remove air from the condenser of a steam engine (Chunnanond & Aphornratana, 2004).

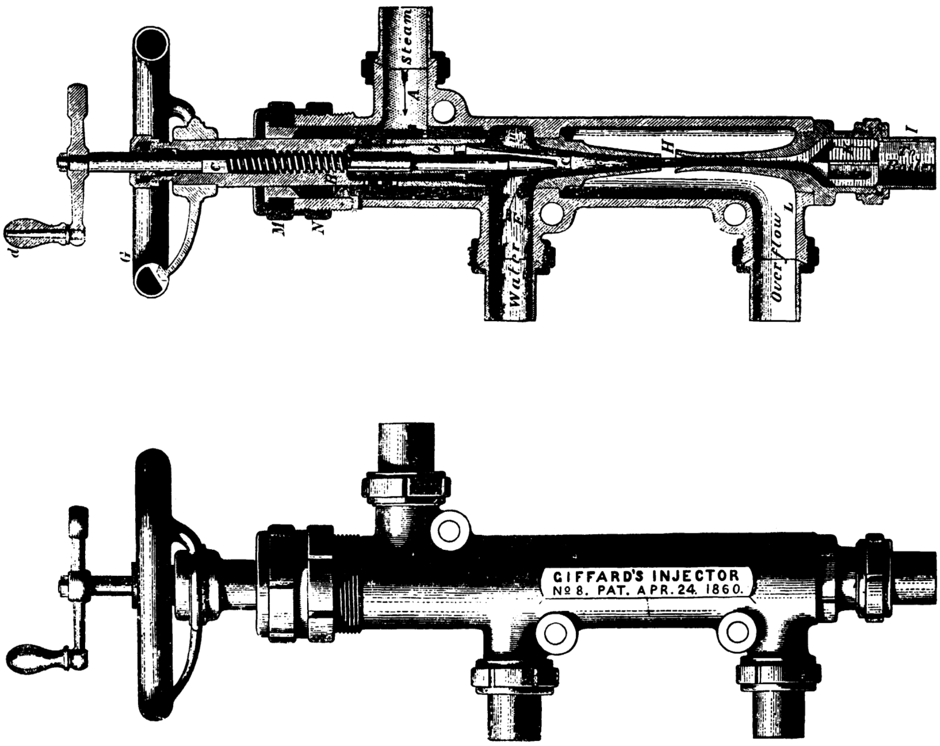

Figure 1.2 Cross-sectional detail of the injector modified in 1859 by Henri Giffard, where the mass flow of the primary fluid was controlled by a needle (Kranakis, 1982)

In 1910, The use of the ejector in the vapor compression refrigeration cycle was made by Leblanc (Leblanc, 1910). Through the proposed vapor compression refrigeration cycle, steam was widely used at that time; obtaining cooling effect using renewable energy or waste heat became popular for air- conditioning of large buildings and railway vehicles. The ejector, which was patented by Gay in 1931 (Gay, 1931), was proposed for use in order to reduce throttling losses in the expansion valve in the conventional refrigeration cycle. In line with these studies, refrigeration cycles in which an ejector is included are classified under two basic categories—these categories are; (i) heat-driven ejector refrigeration systems and (ii) ejector expansion refrigeration systems. The phase conditions of the refrigerant at the inlet and outlet of the ejectors vary according to the cycles that take place. Accordingly, the main types of ejectors are classified, as shown in Table 1.1 (Elbel & Hrnjak, 2008).

Table 1.1 Classification of different commonly used types of ejectors (Elbel & Hrnjak, 2008)

Type of Ejector	Primary Flow (Driving Flow)	Secondary Flow (Driven Flow)	Outlet flow
Vapor Jet Ejector	Vapor	Vapor	Vapor
Liquid Jet Ejector	Liquid	Liquid	Liquid
Condensing Ejector	Vapor	Liquid	Liquid
Two-phase Ejector	Liquid	Vapor	Two-phase

The type of ejector in this thesis is called a *vapor jet ejector* when it is in the high energy primary fluid is the vapor phase, and the secondary fluid is the vapor phase, as seen in Table 1.1. The outlet flow phase of this ejector type is a vapor. In the vapor jet ejector, the two-phase flow may occur, shock waves possible inside its flow area. Also, it is advantageous to use ejectors in terms of resistance to multi-phase flow conditions, low production/maintenance costs, and no moving parts in refrigeration applications (Scott, Aidoun, Bellache, & Ouzzane, 2008). For this reason, many researchers have focused on the physical mechanism of supersonic ejectors in recent years (Besagni, 2019; Little & Garimella, 2016a).

1.3 Using of Ejector in Refrigeration Applications

Considering actual conditions, the components that provide a reducing effect on the energy consumed are very important. Minimizing the energy consumed in the cooling effect intended for the places, components, and various devices in which refrigeration systems are used is a priority. For instance, the expansion valve used in conventional refrigeration cycles causes system-wide throttling losses. Therefore, it is aimed to increase the performance of the refrigeration cycle by adding an ejector to the conventional refrigeration cycle.

1.3.1 Heat-driven Ejector Refrigeration Cycle

The ejector, which is examined numerically, is added to a conventional refrigeration cycle and takes place in a refrigeration cycle originating from renewable energy or waste heat, etc. In general, the name given to this cycle is the heat-driven ejector refrigeration cycle (HDERC). Although low COP values are obtained compared to other ejector refrigeration cycles, studies are being carried out as it can work with renewable or waste heat sources. The heat-driven ejector refrigeration cycle (HDERC) as shown schematically in Figure 1.3.

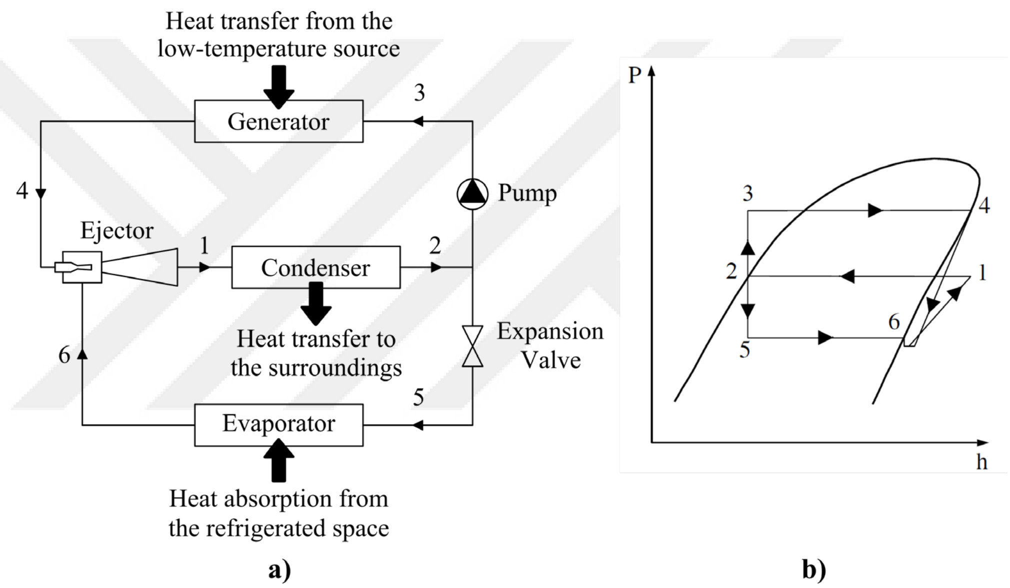

Figure 1.3 Heat-driven ejector refrigeration cycle (HDERC) (a), and P–h diagram (b)

The heat-driven ejector refrigeration cycle is a combination of two loops. The lower cycle (1-2-5-6) is similar to a conventional refrigeration cycle, and the compressor stage is replaced by the upper cycle (1-2-3-4). This configuration is particularly interesting for air-conditioning applications because the entire cycle is mostly driven by low-grade energy (heat input into the generator). Besides, overheating can be added after the evaporator and generator in HDERC applications. So that the fluid in the ejector remains in the superheated (vapor) phase. This situation was not shown in the general cycle schematic. Thus, the supersonic ejector with well-performing single-phase flow is obtained, and this is the crucial parameter for efficient HDERC (Fang, Croquer, Poncet, Aidoun, & Bartosiewicz, 2017).

1.3.2 Ejector Expansion Refrigeration Cycle

The share of air conditioning and refrigeration applications in global energy consumption is continually increasing. For this reason, investigations on alternative refrigeration applications that perform better and have low energy consumption are of great importance. Accordingly, another cycle containing an ejector that has been widely studied in the literature is the ejector expansion refrigeration cycle (EERC). Unlike the conventional vapor compression refrigeration cycle, the ejector expander cycle is created by adding the ejector instead of the expander valve in the cycle. Thus, it is aimed to prevent the negative effect of throttling losses on the expansion performance on the expansion valve. The conventional refrigeration cycle and ejector expander refrigeration cycle are schematically presented in Figure 1.4.

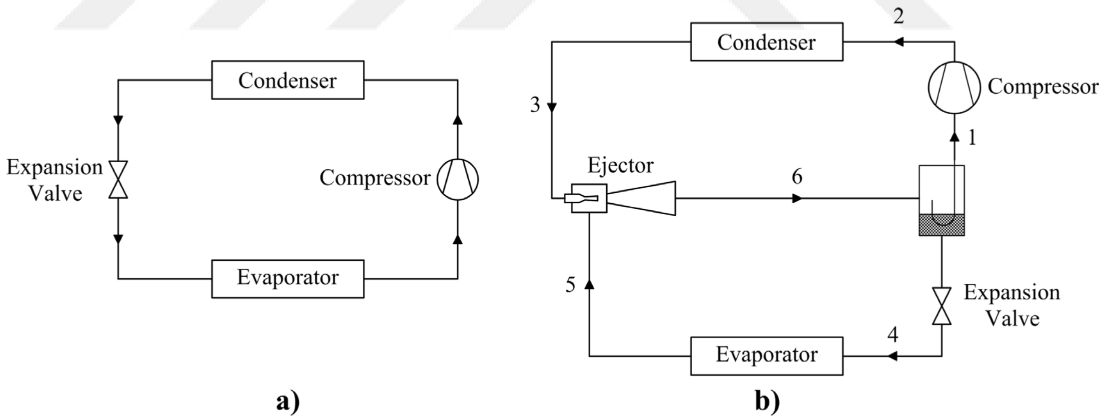

Figure 1.4 Schematic representation of the vapor compression refrigeration cycle (a), and ejector expansion refrigeration cycle (b)

Considering the general working principle of the EERC, the saturated vapor on the vapor side of the liquid-vapor separator was delivered to the compressor. It was isentropically compressed in the compressor, with the acceptance of an ideal cycle. The supercritical motive fluid was transferred to the primary nozzle of the ejector and expanded isentropically to the mixing pressure. Subsequently, the heat was rejected isobarically from the fluid delivered to the condenser (or gas cooler). The observed metastable effects in the dual-phase flow caused by the flashing effect are observed. The high-speed two-phase fluid passing through the primary nozzle transmits momentum transfer to the vapor phase fluid coming from the evaporator, and traction was provided. Shock effects are also observed in the primary and secondary fluid mixed in the ejector mixing section. The mixed-phase fluid formed at the outlet of the ejector was transmitted back to the liquid-vapor separator. Two different mixing processes depend on the specific geometry of the ejector. It was assumed that this mixing process occurs at constant pressure or constant cross-sectional area. (Elbel & Hrnjak, 2008).

1.4 Numerical Modelling of the Ejector in Heat-driven Ejector Refrigeration Cycle

Heat-driven ejector refrigeration cycle and ejector expansion refrigeration cycle configurations are mostly known cycles in the literature related to refrigeration applications. When the overall performance improvement is to be investigated, it is necessary to construct the model of the ejector elaborately in the cycle under consideration since the ejector is the critical component. Hence, to better comprehend the performance evaluation of the heat-driven ejector refrigeration cycle, it is crucial to analyze the flow within the ejector for the operating conditions and design parameters. As a result, this thesis study focused on the vapor jet (supersonic) ejectors used in the heat-driven ejector refrigeration cycle.

Most of the studies in the literature are focused on the performance evaluations of the supersonic ejectors by means of the global parameters such as the entrainment ratio (w), Mach number, and pressure distributions/contours. Studies were exemplified below to present literature findings of the flow characteristics of the ejector at on-design and off-design conditions, the investigations based on the geometrical parameters, and modeling of the vapor jet ejectors. The optimum performance of the supersonic ejectors is found near the critical point. It is supported by Mach number and pressure distribution along with the ejector and Mach contours of the flow structures (Wu, Zhao, Zhang, Wang, & Han, 2018; Allouche, Bouden, & Varga, 2014). Beyond the critical mode of the supersonic ejector (off-design condition), the three-dimensional model becomes more precise than the two-dimensional model, which is illustrated with entrainment ratio and Mach number contours (Mazzelli & Milazzo, 2015). In the sub-critical mode, the ejector is unstable, and a slight increase of back-pressure would affect the system performance negatively (Rusly, Aye, Charters, & Ooi, 2005). At the off-design operation condition, a back pressure higher than the critical pressure of the ejector occurs, and the entrainment ratio of the ejector is highly sensitive to the changes in the downstream pressure (Sriveerakul, Aphornratana, & Chunnanond, 2007a).

The second oblique shock series move upstream towards the first oblique shock series when the downstream pressure becomes higher than the critical pressure. Only one form of the oblique shock appears in the mixing section as a result of the combination of the first and second shock series. This movement concerned with the second oblique shock series could disturb the entrainment ratio since it affects the choked condition of the secondary flow (Sriveerakul, Aphornratana, & Chunnanond, 2007b). On the other hand, when the downstream pressure value is gradually reduced to the critical pressure of the ejector, the entrainment ratio increases and reaches a maximum value (Hemidi, Henry, Leclaire, Seynhaeve, & Bartosiewicz, 2009). In this operation condition, the ejector performs on-design condition, and both primary and secondary flow is choked flow in the mixing section. The expanded wave of the jet stream takes shape over-expanded or under-expanded waves at the exit plane of the primary nozzle (Ruangtrakoon, Thongtip, Aphornratana, & Sriveerakul, 2013). The characteristic of the over-expanded or under-expanded wave in the mixing section of the ejector is directly related to the ejector performance. The shock diamond occurs in the case of both under-expanded and over-expanded waves and acts like a wall (Lamberts, Chatelain, & Bartosiewicz, 2018; Karthick, Rao, Jagadeesh, & Reddy, 2016). Adjacent to the shock diamond, shear stress is very high due to the higher momentum transfer that may cause intense turbulent mixing outside of the primary jet core (Besagni, Mereu, & Inzoli, 2016).

The performance of the ejector can be increased with an appropriate operation condition in the critical mode (Rusly et al., 2005). In addition to the operational conditions, the geometric parameters of the mixing section could also drastically change the ejector performance. The optimum nozzle position and the converging duct angle of the mixing section (θ_{conv}) are able to increase the efficiency of the ejector more than 90% (Watanawanavet, 2005). The optimum position of the primary nozzle is established with the entrainment ratio and Mach number profiles, the path lines of the primary nozzle jet and the critical pressure profile at the ejector exit (Zhu, Cai, Wen, & Li, 2009; Eames, Ablwaifa, & Petrenko, 2007). The optimum position of the primary nozzle is related to the minimum pressure in the suction chamber of the ejector (Yapıcı, Ersoy, Aktoprakoğlu, Halkacı, & Yiğit, 2008). In the case of the reducing distance between the primary nozzle and constant area of the mixing section, the performance of the ejector decreases (Riffat, Gan, & Smith, 1996). Further increase of the convergence angle may affect the increase of the static pressure inside the mixing section and affects the entrainment ratio of the ejector (Utomo, Ji, Kim, Jeong, & Chung, 2008) strength of oblique shocks (Little & Garimella, 2016b).

The shadowgraph technique was employed to understand the flow characteristic of the ejector and the effect of the turbulence model (Little, Bartosiewicz, & Garimella, 2015). Both k-ω SST and k-ε RNG were able to predict the global parameter of the ejector, but k-ε RNG was found to be less accurate to capture a detailed flow physics (Fang et al., 2017). Momentum, energy, and exergy tube analysis tool was used in order to investigate the transport phenomena within the ejector (Lamberts, Chatelain, & Bartosiewicz, 2017). The mechanism of the entropy generation was explained in terms of the low viscous dissipation, viscous fluctuation-dissipation, and heat transfer. Most of the entropy generation was observed near the exit of the constant area section, where strong secondary oblique shocks were observed. The second most significant entropy generation is determined at the mixing location of the primary and secondary flow (Sierra-Pallares, Del Valle, Carrascal, & Ruiz, 2016; Banasiak et al., 2014).

Furthermore, the effective area of the secondary flow is rarely discussed in the ejector studies for flow structures, which is one of the motivations of this study.

Increasing the pressure of the secondary flow decreases the strength of the first oblique shocks. Therefore, weak oblique shocks in the mixing section improve the efficiency of the ejector. This phenomenon was related to the mixing efficiency between the primary and secondary flow (Zhu & Jiang, 2014). Similarly, increased efficiency was related to kinetic energy transfer between the primary and the secondary fluid flows (Zhu et al., 2009). The boundary layer thickness and its relationship with the efficiency were discussed via velocity contours at various cross-sectional planes of the mixing section at various motive flow pressures (Arun, Tiwari, & Mani, 2017). It was concluded that the increased motive pressure also increased momentum transfer between the primary and secondary flows, thereby reducing the effect of the boundary layer.

It was stated that increasing the expansion angle produces a larger cross-sectional area of the primary jet flow. Hence, the effective area of the secondary flow is reduced (Ruangtrakoon et al., 2013; Sriveerakul et al., 2007a). Even though the primary flow has much more momentum, it could not always be said that the secondary mass flow rate increases because of the reduced effective area of the secondary flow. The measurement of the exact value of the effective area is not an easy task (Ruangtrakoon et al., 2013) because the mixing process between the primary and secondary flow gradually starts at the exit of the primary nozzle and continues until two jets is fully-mixed (Allouche et al., 2014). However, it can be assessed with a sonic line and dividing streamlines (Lambert et al., 2017; Lamberts et al., 2018). Between the sonic line and the dividing streamline, the secondary flow reaches sonic flow conditions (Lamberts et al., 2018).

Rusly et al. (2005), using the CFD method, numerically examined the ejector in the vapor compression refrigeration cycle under different operating conditions. Numerical studies have been confirmed by experimental studies. Through the validated numerical model, the operating conditions outside the experimental range and the effect of the change of the area ratios were examined. In line with their findings, it was emphasized that the shock effect seen in the flow inside the ejector and primary nozzle exit position is an essential design parameter for the ejector.

Sriveerakul et al. (2007a, 2007b), was investigated the use of CFD to determine the performance of the ejector in refrigeration applications, numerically. In the first step of the studies, the ejector performance was determined under different working conditions and geometric dimensions by means of the experimentally validated numerical model. In the subsequent studies, the results obtained on the oblique shock, mixing behavior, Choke flow and jet core occurring in the flow in the ejector are presented. It was stated that the use of Computational fluid dynamics is an effective method for analyzing the flow and mixing process in the ejector, as well as the ejector performance parameters such as the obtained entrainment ratio.

Yapıcı et al. (2008) experimentally investigated the performance of a heat-driven ejector refrigeration cycle using R123 as refrigerant under different operating conditions with choking in the mixing section of the ejector. Within the scope of experimental studies, six different ejector configurations were created by the selected area ratios. In the ejector studies, the area ratio was generally defined as the ratio of the area of the mixing section to the area of the primary nozzle throat. They stated that the condenser pressure at the outlet of the ejector should be selected appropriately to examine the secondary flow choking. In addition, it was emphasized that the experimental performance of the system increases when the operating conditions tested are different compression pres ratios($\prod_{comp}$) and generator temperature for optimum values.

Varga, Oliveira, & Diaconu (2009a) considered the effect of the steam jet ejector area ratios, nozzle exit position (*NXP*), and the length of the fixed area mixing section on the entrainment ratio of the ejector. In accordance with the obtained results, the optimum area ratio was obtained depending on the working condition. It was suggested to use spindles in the primary nozzle to change the area ratio and fine-tune primary mass flow rate. In the other parameters examined, the effect of the nozzle exit position (*NXP*) on the entrainment ratio and the critical back pressure at the ejector outlet was stated to be a more effective parameter compared to the length of the constant area mixing section.

Determination of the ejector section efficiencies was commonly used in theoretical models. Section efficiencies of the ejector are generally determined based on specific assumptions and experimental studies. Varga, Oliveira, & Diaconu (2009b) determined the section efficiencies for the primary nozzle section, secondary flow inlet section, mixing section, and diffuser using the CFD model in their study. In the numerical study created, the ejector was modeled as two-dimensional axisymmetric, and water was used as a working fluid. In order to determine the working conditions of the ejector, an air conditioner application using solar energy was chosen as the external heat source. Depending on the determined operating conditions, they obtained the optimum area ratio. In the evaluation made in terms of section efficiency, it was stated that even if the efficiency of the primary nozzle can be evaluated as stable, other ejector partial efficiencies are directly dependent on the operating conditions.

Ruangtrakoon et al. (2013) used the CFD method to investigate the effect of the primary nozzle of the ejector in the steam jet refrigeration cycle on the ejector performance. Eight different primary nozzle geometries were studied, and other geometric dimensions that comprise the ejector were kept constant. They used the entrainment ratio, pressure distribution of the primary fluid, and the Mach number contour graphs to compare the effects resulting from the change of the primary nozzle geometry. It was stated that the shock positions occurring in the ejector flow, and the angle of expansion of the primary fluid significantly affect the performance of the ejector.

Varga, Lebre, & Oliveira (2013) were presented for different positions of a spindle placed in the primary nozzle of the ejector in the 1 kW refrigeration cycle using R600a and R152a refrigerants. In the selection of refrigerant, low environmental impact, and good performance in the use of solar thermal energy as the primary energy source were considered. It was emphasized that the results obtained due to different spindle positions increase performance for low condenser pressure values in the appropriate spindle position compared to the fixed geometry ejector.

Wu, Liu, Han, & Li (2014) have demonstrated the effect of the geometric parameters of the mixing section of the steam ejector on performance using the CFD method. The effect of the converging duct angle and the length of the constant area mixing section, which are the two sub-sections forming the mixture section of the ejector, has been presented to the flow characteristics in the ejector. It was concluded that in order to obtain the best-obtained entrainment ratio value, the optimum value of the converging duct angle and length of the constant area mixing section should be determined.

Omidvar, Ghazikhani, & Razavi, (2016) conducted numerical studies in order to obtain the optimum geometry of the ejector in the solar thermal refrigeration system and to examine the critical flow behaviors that lead to decrease the ejector performance. Results for different primary nozzle positions and condenser temperatures are discussed. They stated that entropy production occurs when the condenser temperature is higher than the critical temperature in the ejector performance curve. Also, for the opposite situation, it was stated that the shock effect in the ejector flow is the main parameter. As a result, it was concluded that there was a significant correlation between entropy production and ejector performance. In this way, the performance of the ejector increase up to 37% was achieved.

Wang, Yan, Wang, & Li (2017) examined the performance of the ejector in the refrigeration application using R134a as the refrigerant using the CFD method and was validated experimentally. The effect of geometric parameters of the primary nozzle on ejector performance was studied. In addition to the length and angle of the primary nozzle converging/diverging sections, results related to the surface roughness were obtained in terms of the entrainment ratio. In parallel with the numerical results, it was concluded that the effect of the primary nozzle throat and divergence section on the entrainment ratio was significant compared to the other geometric parameters was studied.

Sierra-Pallares et al. (2018) proposed a methodology for optimizing the long-tapered mixing section of the ejector due to the generation of entropy in the flow. The baseline geometry was created through a one-dimensional model by dividing the flow area in the ejector into different subfields. Besides, Experimental data were obtained in the baseline geometry parameters range. Afterward, the parameters created were transferred to the CFD model, and numerical analyzes were carried out for different geometric configurations of the mixing section. Numerical results for baseline and optimized ejector geometry was discussed on comparative. It was concluded that up to 16% performance increase could be achieved with parameter optimization, which is critically determined in terms of design, whereas the ejector outlet pressure remains constant.

Ejector geometries must have appropriate design conditions for different operating conditions and different refrigerants in ejector refrigeration applications. Mohamed, Shatilla, & Zhang (2019) reported that using Hydrocarbon as an alternative refrigerant in ejector refrigeration applications in a hot climate has excellent potential. Accordingly, CFD studies were carried out for different studies and geometric conditions using Pentan from Hydrocarbons. In addition to their CFD results, the Pareto Frontier performance curve has been proposed for the design and operation of the Hydrocarbon ejector based on the compression ratio and mass flow rate. It has been reported that the effect of the ejector area ratio on performance is a critical parameter compared to other geometric parameters, and low area rate values form a high compression ratio.

1.5 Alternative Refrigerants Using in Ejector Refrigeration Cycles

In many refrigeration and air-conditioning applications, including ejector refrigeration cycle, have been carried out using new-generation refrigerants as an alternative to HFC refrigerants. Özgür, Kabul, & Kizilkan (2014) carried out an exergy analysis of vapor compressed cooling systems using R1234yf as an alternative to R1334a. As a result of this change, it is stated that while R1234yf provides a lower exergy removal rate, there is no significant difference in terms of energy efficiency. Zilio, Brown, Schiochet, & Cavallini (2011) obtained experimental results by using R1234yf instead of R134a for the automotive air conditioning system. Using R1234yf, experimental and numerical studies were carried out to obtain similar cooling capacities obtained using R134a. Moreover, general cooling applications, studies in the use of new generation environmentally-friendly refrigerants instead of HFC fluids are used in the literature, even in refrigeration applications with ejector.

For refrigeration systems including supersonic ejectors, the use of HFO refrigerants drop-in replacement of R134a, etc. from HFC refrigerants has become a widespread phenomenon. Lawrence and Elbel (2014) carried out experimentally for Ejector Expansion Refrigeration Cycle using refrigerant as R134a and R1234yf. They obtained the Coefficient of Performance (COP) increase by using R134a and R1234yf for two different evaporator combinations in the refrigeration cycle. According to their results, stated that the evaporator design provides COP improvement for EERC. (Navarro-Esbrí, Moles, & Barragán-Cervera, 2013) present an experimental analysis of R1234yf as a drop-in replacement for R134a. From their experimental results, cooling capacity and COP reductions of 6% to 13% were observed because of refrigerant replacement. However, the presence of an Internal Heat Exchanger (IHX) has been to reduce these reductions by 2% to 6%.

In addition to experimental studies, there are numerical studies in the literature. Fang et al. (2017) obtained numerical results using R1234yf and R1234ze(E) from Hydrofluoroolefin(HFO) as an alternative to R134a for single-phase supersonic ejector geometry. Besides, the effect of mixing the fluids used in specific proportions was also examined. It was stated that if R1234yf and R1234ze (E) fluids are used instead of R134a, it is easier to use R1234yf instead of R134a. On the other hand, if the fluid R134ze (E) was used instead of fluid R134a, it was emphasized that certain modifications should be made for the ejector. According to numerical results, it was concluded that when R1234yf was used, there was 9.6% and 19.8% reduction in COP and cooling power, and 4.2% and 26.6% reduction for R1234ze (E), respectively.

Li, Cao, Bu, Wang, & Wang, (2014) studied thermodynamic analysis in EERC using R1234yf as the refrigerant. According to the results, the cycle performance of the R1234yf and R134a refrigerants were compared. Although it is insufficient compared to R134a in terms of performance, it is stated that R1234yf will be a good alternative.

1.6 Objectives and Methodology of the Thesis

The main purpose of this thesis study is to investigate the effects of using different refrigerants for the selected operating conditions in vapor-jet ejectors and the effects of geometric parameters variations on ejector performance. Various geometric changes based on the nozzle exit position (*NXP*) and the converging duct angle (θ_{conv}) is compared in terms of the entrainment ratio, which is one of the most important global performance parameters. Due to the complex physics of the flow in the mixing section of the vapor-jet ejector and its direct effects on ejector performance, this thesis will discuss the detailed flow structures in the ejector mixing section in addition to the entrainment ratio (w). Shadowgraph technique is as well used to display the first and second shock trains for the critical cases selected for comparisons. Mach Number distributions were compared for the same cases at the symmetry axis of the ejector and the secondary fluid. The strength of the motive jet is analyzed based on the selected cases, and its relationship between the capability of the secondary flow entrainment was discussed. Focusing on the entrainment ratio (w) and the motive jet characteristics were analyzed for different cases.

1.7 Structure of the Thesis

This thesis is comprised of five chapters, as follows.

- In the first chapter titled "Introduction", the main points about the basics of the ejector concept and heat-driven refrigeration cycle were summarized. A comprehensive review of the previous studies about the ejector, thesis objectives, and methodology were explained in the first introductory chapter. Besides, a brief structure of the thesis sections was given.

- The second chapter provides detailed information on the numerical model to analyze the ejector performance and flow through it using the Computational Fluid Dynamics (CFD) method. In this section, which includes the basic design parameters and numerical assumptions that comprise the ejector geometry, the sensitivity of the created numerical model according to the different mesh structure and turbulence model was also revealed. In addition, the results of the verification were presented by comparing the numerical model with other numerical and experimental results in the literature.

- In the third chapter, the main properties and boundary conditions determination of R1234yf and R1234ze (E), which were recommended to be used as an alternative to R134a, were explained. Afterward, the effect of using different refrigerants on ejector performance was investigated by using the boundary conditions determined in line with the refrigerant. Throughout the obtained results, in addition to the mass flow rate, the flow structures in the ejector were discussed.

- Chapter four describes the basic geometry created in the previous section, the effect of the change of two different geometric parameters forming the ejector on the ejector performance was examined. These two geometric parameters; It was determined as the primary nozzle exit position (*NXP*) and the converging duct angle of the mixing section (θ_{conv}). In line with the obtained results, mass flow rates, and flow structures within the ejector are presented comparatively.

- Chapter five summarizes the main aspects of the thesis, concluding remarks, and literature contributions.

- In Appendix-1, the nomenclature is given.

CHAPTER TWO
NUMERICAL MODELLING OF THE EJECTOR THROUGH COMPUTATIONAL FLUID DYNAMICS

2.1 Numerical Method and Computational Model

In this numerical study, the ejector used in the heat-driven ejector refrigeration cycle, was modeled using computational fluid dynamics under a single-phase flow assumption for R134a as the working fluid to investigate the flow characteristics. The computational model was performed with a commercial finite volume solver, ANSYS-Fluent v18.1. The computational domain was established for the two-dimensional axisymmetric flow assumption neglecting three-dimensional effects of the flow features (Lamberts et al., 2017; Zhu et al., 2009; Rusly et al., 2005). The numerical convergence criteria of the governing equations were set to the root-mean-square normalized residual value below the 10^{-6}.

2.2 Computational Domain and Governing Equations

The schematic view of the ejector was displayed, as shown in Figure 2.1 with reference to the study of Del Valle, Jabardo, Ruiz, & Alonso (2014) and Croquer, Poncet, & Aidoun (2016). The ejector model consists of basically four sections as follows; (i) primary nozzle and suction section where primary and secondary fluid flows enter, respectively, (ii) converging duct of the mixing section, (iii) constant area mixing section, and (iv) subsonic diffuser.

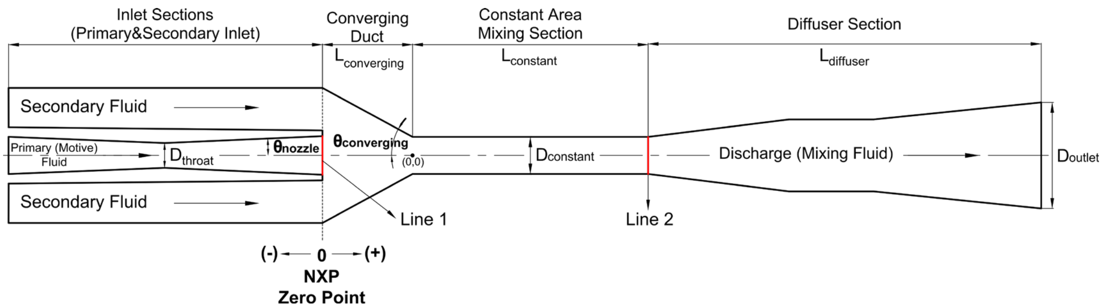

Figure 2.1 Schematic representation of the computational domain for a typical ejector

The working fluid was regarded under the real gas approach that density, specific heat, thermal conductivity, viscosity, and molecular weight were obtained from the REFPROP v9.1 (Lemmon, Huber, & McLinden, 2013) database. The dimensions of the ejector geometry were given in Table 2.1, and these dimensions refer to a base geometry for the parametric simulations of Case 1, which indicates the using R134a with reference ejector geometry. In addition, the boundary conditions used for Case 1 were presented in Table 2.2. Case 1 was used for grid discretization accuracy and mesh independency, turbulence model determination, numerical model verification, and validation study in this Chapter.

Table 2.1 The dimension of the ejector for base geometry (Case 1)

Nozzle diverging angle (θ_p)	1.40°
Converging duct angle (θ_{conv})	29.95°
Primary nozzle throat diameter (D_{throat})	2.00 mm
Converging duct length (L_{conv})	5.38 mm
Constant area mixing section diameter (D_{const})	4.80 mm
Constant area mixing section length (L_{const})	41.39 mm
Diffuser outlet diameter (D_{out})	10.00 mm
Diffuser length (L_{diff})	120.15 mm

Table 2.2 Boundary conditions of Case 1

$P_{p,in}$	2888.8 kPa
$T_{p,in}$	84.34 °C
$P_{s\ in}$	414.608 kPa
$T_{s,in}$	10 °C
$P_{diff,out}$	826.573 kPa
$T_{diff,out}$	32.48 °C

In this thesis study, the geometric parameters are presented by means of the non-dimensionalized designations. The primary nozzle exit position (*NXP*), which is described as the distance between the primary nozzle outlet and the inlet of the converging duct, and the convergence angle of the mixing section (θ_{conv}) were non-dimensionalized with constant area mixing section diameter (D_{const}) and nozzle divergence angle (θ_p), respectively. Also, the origin of the axis must not be confused with the origin of the *NXP* axis, as clearly displayed in Figure 2.1.

Seven different primary nozzle exit positions (*NXP*) were considered, and regarding this parameter, NXP' which is the ratio of *NXP* to D_{const} is investigated for the following values, i.e., 0.00, -0.22, -0.44, -0.66, -0.88, -1.10 and -1.32. Similarly, the converging duct angle of the mixing section (θ_{conv}) values are analyzed through the medium of the dimensionless parameter, θ' which is the ratio of θ_{conv} to θ_p. These investigated θ' values are as follows; 5.3, 7.1, 8.9, 10.7, 12.4, 14.2, 17.9, 19.6, 21.4, and 23.2. Moreover, the x-coordinate and y-coordinate values of the ejector geometry were also divided by D_{const} to obtain the x' and y' values. The x' and y' values refer to the dimensionless positions in the figures of the results obtained in line with this thesis study.

The governing equations are solved using the COUPLED algorithm for the steady-state compressible flow. The advection and diffusion terms of the governing equations were discretized with the second-ordered upwind and second-ordered central difference scheme, respectively. The governing equations for continuity, momentum, and energy used in the computational fluid dynamics (CFD) analyses under the above-given assumptions are as follows;

The continuity equation,

$$\frac{\partial}{\partial x_i}(\rho V_i) = 0 \tag{2.1}$$

The momentum equation,

$$\frac{\partial}{\partial x_j}\left(\rho V_i V_j\right) = -\frac{\partial P}{\partial x_i} + \frac{\partial \tau_{ij}}{\partial x_j} \tag{2.2}$$

The energy equation,

$$\frac{\partial}{\partial x_i}[(V_i(\rho E + P)] = \vec{\nabla} \cdot \left(k_{eff}\frac{\partial T}{\partial x_i}\right) + \vec{\nabla} \cdot [V_j(\tau_{ij})] \tag{2.3a}$$

With

$$\tau_{ij} = \mu_{eff}\left(\frac{\partial V_i}{\partial x_j} + \frac{\partial V_j}{\partial x_i}\right) - \frac{2}{3}\mu_{eff}\frac{\partial u_k}{\partial x_k}\delta_{ij} \tag{2.3b}$$

In addition to continuity, momentum, and energy governing equations, the governing equations of the turbulence model to be used are presented in Chapter 2.4 - Turbulence Model Determination.

The inlet boundary conditions for the primary and secondary fluid flows were specified the pressure-inlet type. Meanwhile, the outlet of the ejector was set to the pressure-outlet type of the boundary condition. The turbulence intensity and the eddy viscosity ratio at the inlet boundaries were prescribed 5% and 10 for a fully developed circular inlet condition, respectively (Sierra-Pallares et al., 2018). The outlet boundary condition was specified as the pressure-outlet type. No-slip shear condition and adiabatic flow assumption were used (Sierra-Pallares et al., 2018).

2.3 Grid Discretization Accuracy and Mesh Independency

The commercial software ANSYS ICEM v18.1 is used to build the structured mesh grid. It is necessary to determine the cell type and the number of grid elements in order to construct the numerical model. The spatial grids were adequately refined finite volume grids to capture the spatial flow features, especially series of the shocks. The grids were generated about 200000 structured quadrilateral elements. Furthermore, the numerical errors were directly related to the mesh quality, while the computational domain was created. Hence, in this study, the maximum cell skewness below 0.33, orthogonal quality higher than 0.78, and the maximum growth rate of 20% were used.

In addition, an elementary mesh independence study was conducted to determine the number of elements constituted the computational domain and to demonstrate the reliability and accuracy of numerical work. Therefore, four different mesh structures were created and named as *Mesh 1*, *Mesh 2*, *Mesh 3*, and *Mesh 4*. The results obtained for each mesh structure solution are given in Table 2.3 and Table 2.4. Mesh structures in Table 2.3 and Table 2.4 were compared with each other by calculating entrainment ratio (w), the area-weighted average of the pressure, and velocity values on Line 1 and Line 2, as depicted in Figure 2.1.

Table 2.3 Results of mesh independency analyses in terms of entrainment ratio (w)

Mesh No.	Cell Number	Entrainment Ratio (w) [-]	Variation (w) (%) [-]
Mesh 1	67551	0.3978	-
Mesh 2	130351	0.3981	0.09
Mesh 3	204367	0.3987	0.14
Mesh 4	293190	0.3992	0.12

Table 2.4 Results of mesh independency analyses in terms of velocity (V) and pressure (P)

Line 1					
Mesh No.	**Cell Number**	**Velocity [m/s]**	**Variation (V) (%) [-]**	**Static Pressure [Pa]**	**Variation (P) (%) [-]**
Mesh 1	67551	258.20	-	418988.34	-
Mesh 2	130351	257.80	0.15	419527.82	0.13
Mesh 3	204367	257.52	0.11	420044.63	0.12
Mesh 4	293190	257.30	0.09	420425.96	0.09
Line 2					
Mesh No.	**Cell Number**	**Velocity [m/s]**	**Variation (V) (%) [-]**	**Static Pressure [Pa]**	**Variation (P) (%) [-]**
Mesh 1	67551	103.96	-	617321.90	-
Mesh 2	130351	105.04	1.03	613590.67	0.60
Mesh 3	204367	105.59	0.53	611267.73	0.38
Mesh 4	293190	105.93	0.32	610052.27	0.20

The Grid Convergence Index (GCI) is a method used in many numerical studies to determine the grid discretization accuracy and the numerical error depending on the grid size interval. The equations used in the GCI analysis were derived from the Richardson extrapolation method in order to estimate the discretization error (Celik, Ghia, & Roache, 2008). Three different grids must be used for the GCI study. Mesh 2, Mesh 3, and Mesh 4 used previously in the mesh independency study were selected for the analysis at issue.

$$h = \left[\frac{1}{N} \sum_{i=1}^{N} (\Delta A_i) \right]^{\frac{1}{2}} \quad (2.4)$$

Where ΔA_i is the area of i^{th} mesh cell, and N is the total number of cells in the computational domain. Another required parameter for the analysis is called the apparent order (p) and calculated as

$$p = \frac{1}{\ln r_{23}} |\ln|\varepsilon_{34}/\varepsilon_{23}| + q(p)| \quad (2.5a)$$

$$q(p) = \ln\left(\frac{r_{23}^{p} - s}{r_{34}^{p} - s} \right) \quad (2.5b)$$

$$s = (1)[sgn(\varepsilon_{34}/\varepsilon_{23})] \quad (2.5c)$$

Where r is the grid refinement factor, and ε is the difference of any investigated parameter between the grids. The refinement factor is defined as the ratio of h_{coarse} to h_{fine}. If the calculated refinement factor value is constant, i.e., r_{34} is equal to r_{23}, $q(p)$ would be calculated as zero. In this study, the value of apparent order (p) was calculated by solving Equation 3.5 with the fixed-point iteration method since the r_{34} and r_{23} is equal to 1.198 and 1.252, respectively. As for the calculation of ε, ε_{34} is the difference between φ_3 and φ_4 in the respective order of the subscript of ε and ε_{23} is defined similarly. φ_4, φ_3, and φ_2 are obtained for different grid solutions. The approximate relative errors (e) and the grid convergence index (GCI) are calculated through the medium of the following equations.

$$e_a^{34} = \left| \frac{\varphi_4 - \varphi_3}{\varphi_4} \right| \quad (2.6)$$

$$e_a^{23} = \left|\frac{\varphi_3 - \varphi_2}{\varphi_3}\right| \tag{2.7}$$

$$GCI_{fine}^{34} = \frac{1.25e_a^{34}}{r_{34}^p - 1} \tag{2.8}$$

$$GCI_{coarse}^{34} = \frac{1.25e_a^{34}r_{34}^p}{r_{34}^p - 1} \tag{2.9}$$

$$GCI_{fine}^{23} = \frac{1.25e_a^{23}}{r_{23}^p - 1} \tag{2.10}$$

$$GCI_{coarse}^{32} = \frac{1.25e_a^{23}r_{23}^p}{r_{23}^p - 1} \tag{2.11}$$

The values of the analyzed parameters calculated at seven different points within the ejector were determined on the symmetry axis for the structures of Mesh 4 (fine), Mesh 3 (medium), and Mesh 2 (coarse). The values were displayed in Table 2.5 and named as φ_4, φ_3, and φ_2. The maximum GCI_{fine} value obtained by using the equations in the GCI study is 1.447%, and the minimum GCI_{fine} value is 0.004% for velocity magnitudes. When the results were analyzed according to the static pressure, the maximum GCI_{fine} value is 0.979%, and the minimum GCI_{fine} is approximately 0.000086%. The maximum discretization error for fine grid evaluation was calculated as ±0.488 m/s, with multiplying 33.37 by ±1.447% for velocity magnitude value. The static pressure value, which was another selected variable, was calculated as ±4.153 kPa from the multiplication of 424.18 kPa and ±0.979%. Also, the error range of other selected points was given, as shown in the last column of Table 2.5.

Table 2.5 Results of the grid convergence index (*GCI*) study

Velocity Magnitudes[m/s]											
x/D_{const}, y=0	φ_4 V_4	φ_3 V_3	φ_2 V_2	ε_{34}	ε_{23}	e_{34}	e_{23}	p	GCI_{fine}^{34} [%]	GCI_{coarse}^{32} [%]	**Error (Fine)**
-9.60	33.73	33.75	33.77	0.0220	0.0261	0.0007	0.0008	0.303	**1.447**	1.466	**±0.488**
-5.38	122.37	122.61	122.83	0.2361	0.2243	0.0019	0.0018	1.727	**0.659**	0.711	**±0.807**
-1.12	265.86	265.93	265.85	0.0701	-0.0789	0.0003	0.0003	0.580	**0.299**	0.303	**±0.794**
0.00	265.24	265.27	265.11	0.0280	-0.1559	0.0001	0.0006	7.901	**0.004**	0.088	**±0.011**
11.33	125.17	125.92	126.30	0.7446	0.3764	0.0059	0.0030	5.859	**0.396**	0.510	**±0.495**
19.46	22.83	22.77	22.86	-0.0561	0.0927	0.0025	0.0041	2.411	**0.564**	1.216	**±0.129**
33.65	6.35	6.30	6.41	-0.0550	0.1073	0.0087	0.0170	3.187	**1.392**	4.162	**±0.088**
Static Pressure[kPa]											
x/D_{const}, y=0	φ_4 P_4	φ_3 P_3	φ_2 P_2	ε_{34}	ε_{23}	e_{34}	e_{23}	p	GCI_{fine}^{34} [%]	GCI_{coarse}^{32} [%]	**Error (Fine)**
-9.60	2789.62	2789.50	2789.35	-0.1253	-0.1481	0.0000	0.0001	0.333	**0.091**	0.092	**±2.532**
-5.38	1862.00	1859.14	1856.51	-2.8635	-2.6261	0.0015	0.0014	1.955	**0.455**	0.496	**±8.463**
-1.12	424.18	423.76	424.24	-0.4127	0.4711	0.0010	0.0011	0.649	**0.979**	1.024	**±4.153**
0.00	427.63	427.49	428.41	-0.1404	0.9171	0.0003	0.0021	8.601	**0.011**	0.314	**±0.047**
11.33	755.12	754.86	755.04	-0.2597	0.1855	0.0003	0.0002	2.195	**0.088**	0.079	**±0.668**
19.46	820.39	820.37	820.37	-0.0148	6.9E-06	1.8E-05	8.4E-09	56.40	8.6E-08	1.1E-06	7.1E-07
33.65	826.57	826.57	826.57	-1.5E-04	-7.5E-05	1.8E-07	9.0E-08	5.774	1.2E-05	1.6E-05	9.9E-05
$\boldsymbol{h_4} = 0.183\ mm\ (Fine), \boldsymbol{h_3} = 0.219\ (Medium), \boldsymbol{h_2} = 0.274\ (Coarse)$											

When the results of the mesh independency study are evaluated, it was seen from Table 2.5 that the solutions obtained with Mesh 3 and Mesh 4 have a lower error similar to each other. As a result of the GCI study, Mesh 3 was found to have a low *GCI* value. Besides, Mesh 3 has a lower solution time and memory usage than Mesh 4. Mesh 3 includes approximately 200000 structured elements, and it was significantly refined in the vicinity of the shocks. The structure of the mesh 3 was shown in detail in Figure 2.2.

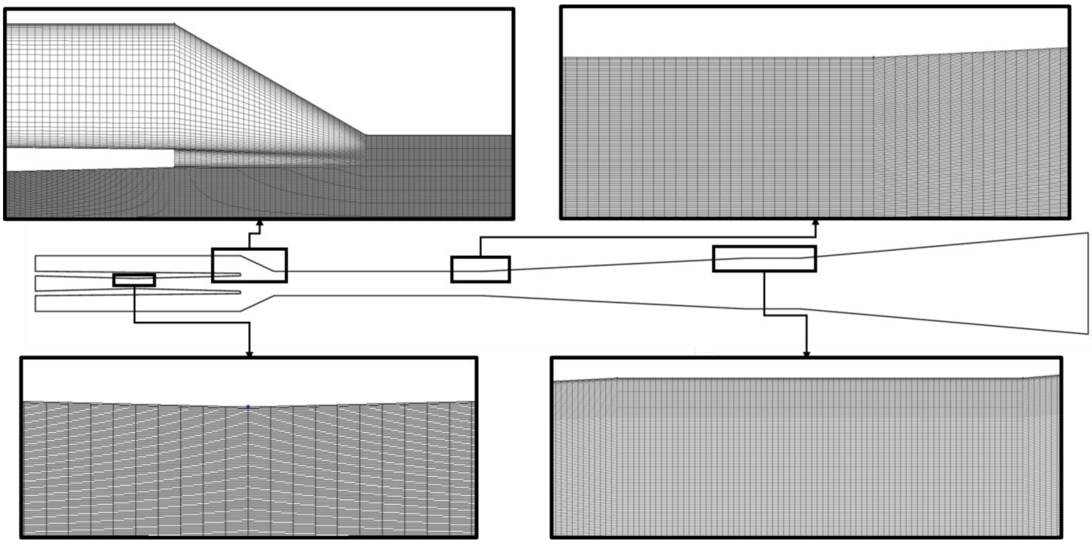

Figure 2.2 Detailed view of the mesh structure of mesh 3b

2.4 Turbulence Model Determination

Preliminary work was carried out to determine the turbulence model to be used in the numerical model. It is seen from the literature that different turbulence models could be used in the numerical models. These are Standard k-ε, RNG k-ε, Realizable k-ε, Standard k-ω, SST k-ω, Spalart-Allmaras, Reynolds Stress, and Transition SST turbulence models. Mazzelli & Milazzo (2015) emphasized that the results obtained by using SST k-ω and Reynolds Stress models were more compatible with the experimental when compared to the other turbulence models. However, there were numerical stiffness and convergence errors when using the Reynolds Stress turbulence model.

Moreover, with reference to Croquer et al. (2016), oblique shock series in the mixing section of ejector were captured better by means of the SST k-ω model compared to the other turbulence models. Although the best results were obtained by using the SST k-ω turbulence model, it was observed that the time required for the calculations was too long. According to Besagni & Inzoli (2017), the SST k-ω model yielded the best results for the numerical verification of global and local flow parameters obtained from the experimental results. The authors stated that for future numerical studies concerned with the ejector, the use of the SST k-ω model was proposed. However, Varga, Soares, Lima, & Oliveira, (2017) proposed two turbulence models, namely Transition SST and standard k-ε having modified model constants, to achieve better COP and critical back pressure estimations with respect to experimental studies.

In order to obtain accurate results from the turbulence models, it is crucial to determine the first layer thickness in line with the appropriate y plus (y^+)value depending on the turbulence model to be used. The velocity profile formed under the laminar flow condition develops almost linearly compared to the turbulent flow. In turbulent flow, especially in high Reynolds numbers, the development of the flow velocity profile from the wall takes place in the form of instantaneous and parabolic curves. Therefore, the velocity profile of the turbulent flow developing from the wall should be examined in detail near the wall layer. In this sense, arranging the mesh structure in the near-wall region improves the accuracy of numerical analysis.

The first layer thickness obtained based on two different y^+ values are compared in Figure 2.3. The coarse structure through the wall in the y-direction, as shown in Figure 2.3a. Besides, the fine mesh structure was shown in Figure 2.3b. In line with the turbulence models, the initial wall heights, and the elements that follow can be selected as in Figure 2.3a or Figure 2.3b. The solution is provided by using wall function assumptions in addition to the turbulence models that have high y^+ and thus, high first layer thickness mesh structure as in Figure 2.3a. However, Figure 2.3b represents a more acceptable mesh structure for capturing the logarithmic velocity profile formed from the wall of turbulent flow.

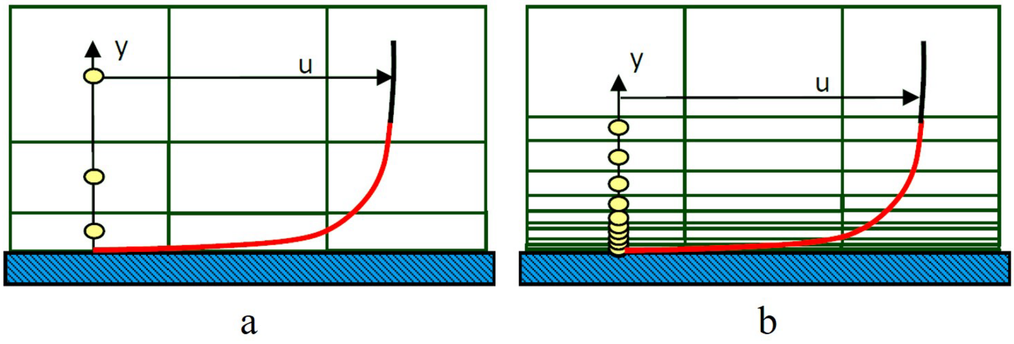

Figure 2.3 Coarse mesh structure (high y^+ value) (a) b. fine mesh structure (low y^+ value) (b) through the wall (ANSYS, 2016)

The calculation of the first layer thickness, which is suitable for the desired y^+, is given by Equation 2.12.

$$y = \frac{y^+ \mu}{U_T \rho} \tag{2.12}$$

Where y^+ is the dimensionless value, which desired for different turbulence models and flows conditions. ρ is density and μ dynamic viscosity of the fluid. U_T is frictional velocity and can be calculated by using Equation 2.13.

$$U_T = \sqrt{\frac{\tau_w}{\rho}} \tag{2.13}$$

τ_w is wall shear stress and is calculated with Equation 2.14.

$$\tau_w = \frac{1}{2} \rho C_f U^2 \tag{2.14}$$

Where U is freestream velocity, and C_f is the skin friction coefficient. C_f is obtained by using Equation 2.15 for internal flows (Date, 2005).

$$C_f = 0.079 Re^{-0.25} \tag{2.15}$$

In the analysis based on the near-wall functions, two mesh structures with the same number of elements and different first wall height were used. Two mesh structures were created, having the same number of elements of the Mesh 3 structure, which is selected as a result of the mesh independency and GCI studies. The mesh structure used for standard-wall-function, scalable-wall-function, and non-equilibrium-wall-function is Mesh 3a. In this mesh structure, the y^+ value, which is called the unitless wall height, is chosen as approximately 35, and the first wall height was calculated accordingly. The mesh structure used for Enhanced Wall Treatment wall functions is named as Mesh 3b. In this mesh structure, the y^+ value was chosen as approximately 1 and so the first wall height was selected to be lower than Mesh 3a. The wall function was not included for the standard k-ω, SST k-ω, and Spalart-Allmaras turbulence models and was directly incorporated into the main equations. For this reason, only one analysis has been done with two mesh structures for these models. In other turbulence models, wall functions were selected and analyzed with an appropriate mesh structure.

Table 2.6 shows the results of numerical analyses through various turbulence models and wall functions. The results were evaluated on the effect of the pressure difference between the ejector primary nozzle inlet and diffuser outlet and the entrainment ratio (w), which is one of the global parameters of the ejector performance. When the results in Table 2.6 were evaluated, in terms of the entrainment ratio (w), it is seen that the least error value was obtained by SST k-ω using Mesh 3b structure with reference to experimental data of Del Valle et al. (2014). The error between the numerical and experimental entrainment ratio (w) obtained by Del Valle et al. (2014) was calculated as approximately 0.126%. When the results were analyzed in terms of the pressure difference between the primary nozzle inlet and outlet of the ejector, it is seen that the variation of the calculated values is around 0.017%. For this reason, the SST k-ω turbulence model and Mesh 3b were selected for parametrical analyses.

Table 2.6 Numerical study results of the sensitivity of the turbulence model and near-wall treatment

<table>
<tr><th rowspan="3">Mesh</th><th rowspan="3">Near-Wall Treatment</th><th colspan="6">Turbulence Models</th></tr>
<tr><th colspan="6">w [-]</th></tr>
<tr><th>Standard k– ε</th><th>Realizable k–ε</th><th>RNG k–ε</th><th>Standard k-ω</th><th>SST k-ω</th><th>Spalart–Allmaras</th></tr>
<tr><td rowspan="3">Mesh 3a, y⁺≅ 35</td><td>Standard Wall function</td><td>0.3946</td><td>0.3921</td><td>0.4058</td><td rowspan="3">0.3959[a]</td><td rowspan="3">0.3987[a]</td><td rowspan="3">0.4111[a]</td></tr>
<tr><td>Scalable Wall Function</td><td>0.3946</td><td>0.3921</td><td>0.4058</td></tr>
<tr><td>Non Equilibrium Wall Function</td><td>0.3951</td><td>0.3925</td><td>0.3959</td></tr>
<tr><td>Mesh 3b, y⁺≅ 1</td><td>Enhanced wall treatment</td><td>0.3939</td><td>0.3913</td><td>0.3941</td><td>0.3958[a,b]</td><td>0.3985[a,b]</td><td>0.4114[a]</td></tr>
<tr><th rowspan="2">Mesh</th><th rowspan="2">Near-Wall Treatment</th><th colspan="6">ΔP=P_{p,in}-P_{diff,out} [kPa]</th></tr>
<tr><th>Standard k– ε</th><th>Realizable k–ε</th><th>RNG k–ε</th><th>Standard k-ω</th><th>SST k-ω</th><th>Spalart–Allmaras</th></tr>
<tr><td rowspan="3">Mesh 3a, y⁺≅ 35</td><td>Standard Wall function</td><td>1966.67</td><td>1966.62</td><td>1966.62</td><td rowspan="3">1966.86[a]</td><td rowspan="3">1966.80[a]</td><td rowspan="3">1966.76[a]</td></tr>
<tr><td>Scalable Wall Function</td><td>1966.67</td><td>1966.62</td><td>1966.62</td></tr>
<tr><td>Non Equilibrium Wall Function</td><td>1966.59</td><td>1966.54</td><td>1966.53</td></tr>
<tr><td>Mesh 3b, y⁺≅ 1</td><td>Enhanced Wall Treatment</td><td>1966.849</td><td>1966.763</td><td>1966.769</td><td>1966.87[a,b]</td><td>1966.77[a,b]</td><td>1966.77[a]</td></tr>
<tr><td colspan="8">[a] Near-Wall Treatment was not selected for the results obtained using Standard k-ω, SST k-ω, and Spalart–Allmaras turbulence models. These turbulence models already have wall function in their own mathematical equations.
[b] The results obtained for k-ω turbulence models were obtained using Low-Re corrections.</td></tr>
</table>

In line with the results obtained using different turbulence models summarized in Table 2.6, the SST k-ω turbulence model and Mesh 3b have been chosen for use in the analyses where the effect of the refrigerant and geometric parameters will be examined. The governing equations of the SST k-ω turbulence model are as Equation 2.16 and Equation 2.17 in general form;

Turbulence Kinetic Energy (k),

$$\frac{\partial}{\partial x_i}(\rho k V_i) = \frac{\partial}{\partial x_j}\left(\Gamma_k \frac{\partial k}{\partial x_j}\right) + G_k - Y_k + S_k + G_b \qquad (2.16)$$

Specific Dissipation Rate (ω),

$$\frac{\partial}{\partial x_i}(\rho \omega V_i) = \frac{\partial}{\partial x_j}\left(\Gamma_\omega \frac{\partial \omega}{\partial x_j}\right) + G_\omega - Y_\omega + S_\omega + G_{\omega b} \qquad (2.17)$$

In these equations G_k, represents turbulent kinetic energy production based on mean velocity gradients. G_ω represents the production of ω. Γ_k and Γ_ω represent the effective diffusivity of k and, respectively. Y_k and Y_ω represent the dissipation of k and ω due to turbulence. S_k and S_ω are user-defined source terms. G_b and $G_{\omega b}$ account for buoyancy terms.

2.5 Numerical Model Verification and Validation

The numerical study of the same ejector conducted by Croquer et al. (2016) was used for comparison as well through the Mach number distribution of the primary fluid flow along the symmetry axis of the ejector, as shown in Figure 2.4. It is seen that an agreement is achieved between similar turbulence models for the same ejector geometry, whose dimensions were specified in this section, with reference to Croquer et al. (2016) and Case 1.

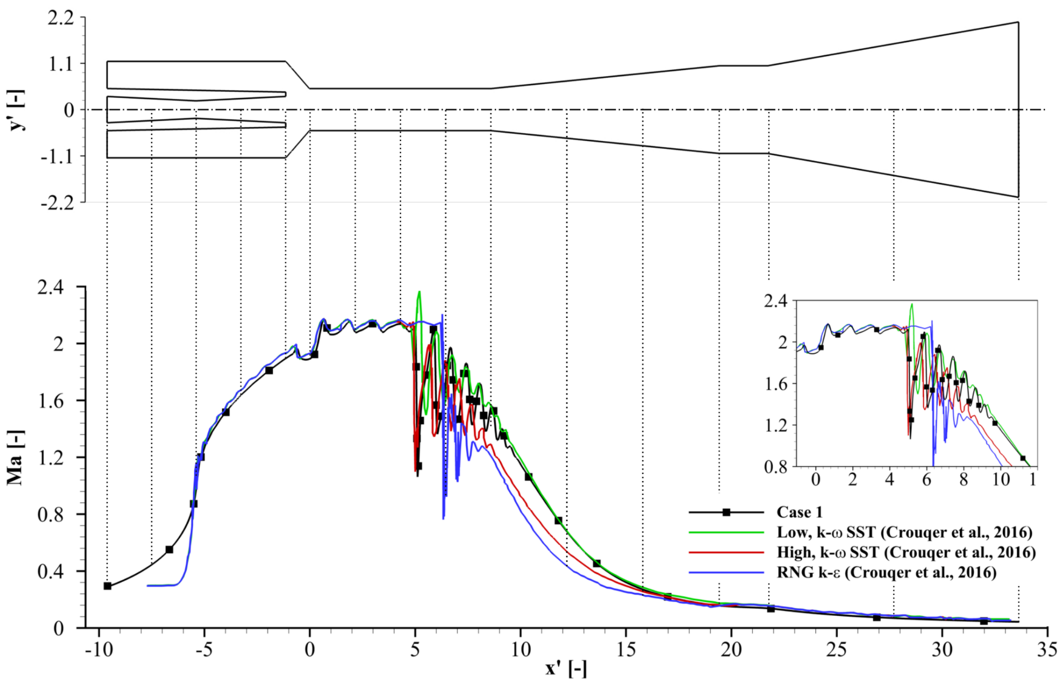

Figure 2.4 Comparison of the Mach Number distribution of the primary flow along the ejector axis between the numerical results of the reference study (Croquer et al., 2016) and the findings of this study

An agreement achieved between the numerical and experimental results in terms of the global parameters such as the entrainment ratio (w) does not guarantee to capture the local flow structures (Hemidi et al., 2009). For this reason, the numerical model is required to be validated by an experimental vertical gradient of the density presented by Lamberts et al. (2017), as shown in Figure 2.5. The boundary conditions and ejector geometry of the experimental study (Lamberts et al., 2017) were directly implemented into the numerical model, and the colormap of the numerical study is adjusted to show the flow structures in detail. The first series of the oblique shocks were located in the vicinity of the primary nozzle in both experimental and numerical study of Lamberts et al. (2017), and these flow structures were captured by the model constructed within this investigation show the validation.

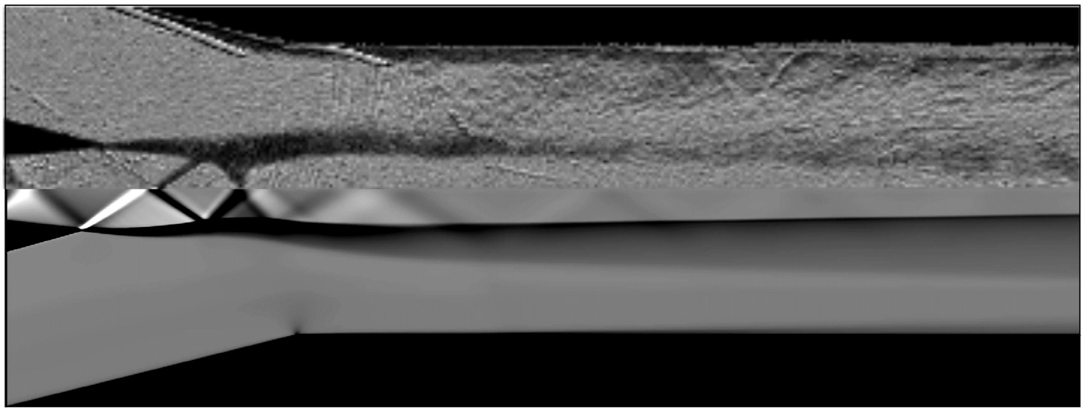

Figure 2.5 Vertical gradient of density field comparison between the experimental study of the reference study (Lamberts et al., 2017) (top) and the established numerical model (bottom)

CHAPTER THREE
INVESTIGATION OF EJECTOR PERFORMANCE FOR VARIOUS REFRIGERANTS

3.1 Refrigerants Selection for Numerical Studies

Chlorofluorocarbon(CFC), Hydrochlorofluorocarbon (HCFCs), and Hydrofluoroolefin (HFO) refrigerants are widely used as working fluid in refrigeration and air-conditioning applications which include an ejector. These refrigerants are currently regulated due to environmental concerns about global warming (Directive 2006/40/EC, 2006; Regulation (EU) No 517/2014, 2014). In line with the Montreal Protocol (1987), Kyoto Protocol (1997), Paris Agreement (2015) and Kigali Amendment (2016), restrictions were applied to the use of CFCs, HCFCs, and HFCs. Type of these refrigerants have a direct effect in case of leakage and release to the environment due to their high Ozone Depletion Potential (ODP) and Global Warming Potential GWP values, although they are stable, non-toxic and flammable. For this reason, as an alternative to the commonly used R134a refrigerant, environmentally friendly fluids such as R1234yf and R1234ze(E), which low GWP value, zero ODP, and excellent life cycle are preferred. Furthermore, R1234yf and R1234ze(E) proposed as an alternative to R134a has similar thermophysical properties. Therefore, when necessary arrangements are made in the system, it can easily be used as an alternative.

In this part of the thesis, the effect of using R1234yf and R1234ze (E), which are new-generation environmentally friendly refrigerants, instead of R134a on the ejector performance was investigated numerically. These are two environmentally-friendly refrigerants compared to R134a due to zero Ozone Depletion Potential (ODP) and very low 100-year Global Warming Potential (GWP_{100}), as shown in Table 3.1. In the literature, it has also been shown that the use of R1234yf or R1234ze(E) instead of R134a has a negative effect on the overall cycle and ejector performance in terms of entrainment ratio (w) (Fang et al., 2017; Navarro-Esbrí et al. 2013; Özgür et al., 2014). For this reason, it was aimed to increase the performance in terms of ejector geometry and working conditions. The results obtained for this section of the thesis was based on the evaluation of flow structures in the ejector and entrainment ratio (w) for the investigated refrigerants.

Table 3.1 Thermodynamic and environmental properties of R134a, R1234yf and R1234ze(E) (ANSI/ASHRAE Standard 34, 2010; Lemmon et al., 2013)

Refrigerants	**R134a**	**R1234yf**	**R1234ze(E)**
Chemical name	1,1,1,2 tetrafluoroethane	2,3,3,3 tetrafluoroprop-1-ene	1,3,3,3 tetrafluoroprop-1-ene
Chemical formula	CF_3CFH_2	$CH_2C{=}CFCF_3$	$CF_3CH{=}CHF$
Molecular weight (g/mol)	102.03	114.04	114.04
Toxicity class (ASHRAE Std 34)	A (low)	A (low)	A (low)
Flammability (ASHRAE Std 34)	A1 (Non-flammable)	A2L (low flammability)	A2L (low flammability)
100-year Global Warming Potential (GWP_{100})	1430	4	7
Ozone Depletion Potential (ODP)	0	0	0
Lifetime in the atmosphere for 1-year	13	0.03	0.05
Normal boiling point (°C)	-26.07	−29.45	−18.97
Critical Temperature (°C)	101.6	94.7	109.36
Critical Pressure (MPa)	4.06	3.38	3.64

3.2 Operating Conditions Determination of the Ejector

In the study of Del Valle et al. (2014) selected as the reference geometry from the literature, R134a was used as the refrigerant, and the boundary condition conditions applied are given in Table 3.2. In addition to this condition, the boundary conditions used for R1234yf and R1234ze (E) are included in Table 3.2 to numerically investigate the effect of using different refrigerants on the ejector performance using the reference ejector geometry. The boundary conditions for R1234yf and R1234ze (E) were determined through the boundary conditions used for R134a with a specific methodology to compare ejector performance. The steps of this methodology are as follows;

i) Generator temperature (Primary inlet temperature) specified for R134a was used for R1234yf and R1234ze(E) by keeping it constant.

ii) The generator vapor pressure (Primary inlet pressure at the saturation condition) for R1234yf and R1234ze(E) at the generator temperature was determined.

iii) The ratio of the generator pressure to the evaporator pressure, expansion ratio, was determined for R134a.

iv) Evaporator pressure (Secondary inlet pressure) was determined using generator pressure and expansion ratio for R1234yf and R1234ze (E).

v) Evaporator temperature (Secondary inlet temperature at the saturation condition) corresponding to the determined evaporator pressure was determined.

vi) Condenser pressure (Ejector outlet pressure) was chosen considering the ejector being in on-design condition (Fang et al., 2017).

Table 3.2 Boundary conditions of the ejector for the selected refrigerants

Refrigerant Name	**$P_{generator}$ [kPa]**	**$T_{generator}$ [°C]**	**$T_{generator}$ [°C] (OH)**	**$P_{evaporator}$ [kPa]**	**$T_{evaporator}$ [°C]**	**$T_{evaporator}$ [°C] (OH)**	**ξ_{exp}* [-]**	**$P_{condenser}$ [kPa]**	**$T_{condenser}$ [°C]**
R134a	2888.8	84.39	-	414.61	10	-	**6.97**	826.6	32.48
R1234yf	2753.93	84.39	94.39	395.25	6.8	16.8	**6.97**	787.9	30.21
R1234ze(E)	2203.75	84.39	94.39	316.29	10.75	20.75	**6.97**	630.6	33

The numerical study was carried out on the experimentally studied ejector geometry in Del Valle et al. (2014) under the working conditions specified in Table 3.2. The numerical study, which was verified and mesh sensitivity, was studied using R134a. Although studies on numerical validation and mesh sensitivity have been performed only for R134a, R1234yf and R1234ze (E) have almost similar characteristics to R134a, as seen in Table 3.1. Accordingly, it has been found appropriate to use in numerical calculations with HFOs using a similar numerical methodology and mesh structure.

3.3 Effect of the Using Different Refrigerants on Ejector Performance

R1234yf and R1234ze (E) proposed to be an alternative to R134a was examined in the generated numerical model, and results related to ejector performance were obtained. In addition, in numerical analysis using R1234yf and R1234ze(E), 10° C overheating was applied for primary nozzle inlet (Generator outlet) and secondary flow inlet (Evaporator outlet) boundary conditions. Thus, the effect of overheating to be applied at the ejector inlets (primary nozzle inlet & secondary flow inlet) was also investigated.

The numerical results obtained using R134a, R1234yf, and R1234ze (E) were compared using entrainment ratio (w), axial Mach Number distributions, and Mach Number contour distributions, which is one of the ejector general performance evaluation criteria. Besides, shadowgraph graphs obtained using the density change gradient are presented for detailed analysis and comparison of shock series occurring in the flow area of the ejector. The results named Case 1, Case 2, and Case 3 are the results obtained using R134a, R1234yf, and R1234ze (E), respectively. Besides, studies with overheating for R1234yf and R1234ze (E) are also designated as Case2* and Case3*. The values obtained as a result of CFD analysis are presented for the mentioned cases in Table 3.3. Primary and secondary fluid mass flow rates ($\dot{m}_p$ and $\dot{m}_s$) of the ejector were presented in detail, and the mass flow rate obtained using these values was also included.

Table 3.3 Comparison of primary and secondary mass flow rates and entrainment ratio of the ejector for R134a, R1234yf, and R1234ze(E) at the operating conditions given in Table 3.2

Case Name	Primary Mass Flow Rate ($\dot{m}_p$) [kg/s]	Secondary Mass Flow Rate ($\dot{m}_s$) [kg/s]	Entrainment Ratio (w) [-]
Case 1	0.03986	0.01589	0.39868
Case 2	0.04035	0.01543	0.38229
Case 2*	0.03775	0.01558	0.41274
Case 3	0.03041	0.01267	0.41675
Case 3*	0.02921	0.01256	0.42998

When the primary and secondary fluid mass flow rates were analyzed for all cases, it can be seen in Table 3.3 that the highest primary flow mass flow value is Case 2, and the highest secondary flow mass flow value is Case 1. However, in the analysis of the general performance parameter of an ejector, the entrainment ratio (w) obtained by the ratio of the secondary fluid mass flow rate to the primary fluid mass flow rate was used. The purpose of the ejectors is essential, how much the secondary fluid is entrained relative to the mass flow of the primary fluid. For this reason, it is seen that all the cases were examined in terms of entrainment ratio (w), and the best performance was obtained in Case 3 *.

In accordance with the use of different fluids, the distribution of Mach number obtained during the x-axis of supersonic ejector was obtained and compared, as shown in Figure 3.1. The most obvious effect of using different fluids in the flow field is to obtain the position of the primary and secondary oblique shock series differently. It can be seen from the instantaneous Mach number changes that the severity of the oblique shock series is different as well. When x'= 5.1, a more massive sudden change was observed in the secondary oblique shock series for Case 1. Secondary oblique shock series appears to occur ahead of the other cases in terms of location. When other cases were examined, shock positions were obtained at the far back for Case 2 and Case 2 * cases where R1234yf was used. It is seen that the cases with approximately Ma=2.2 reaching the highest Mach number are Case 3 and Case 3 * using R1234ze (E).

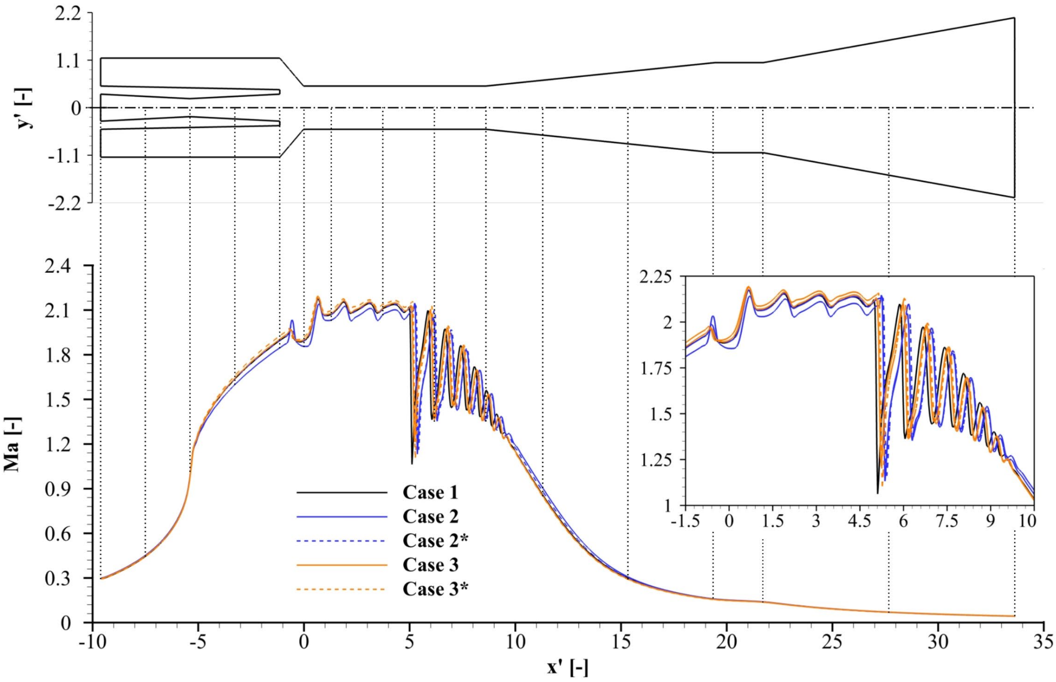

Figure 3.1 Mach number distribution throughout the ejector at the symmetry axis according to different cases

Figure 3.2 is presented to compare the sudden spatial change of Mach Number in an axial sense, as well as the expansion of the primary fluid at the primary nozzle exit and reaching the sonic state. The created Figure 3.2 shows where the fluid in the flow area is sonic and supersonic for different cases. In the Figure 3.2, the subsonic state for the primary and secondary fluid is cropped so that the instantaneous change of Mach number in the flow area is more clearly understood. All cases considering, it is seen that the primary fluid reaches the sonic condition and reaches the supersonic condition in the throat due to the structure of the primary nozzle with converging-diverging geometry. The primary flow discharges from the primary nozzle as an over-expanded wave and the primary and secondary flows reach supersonic flow conditions for all cases. In other words, choked flow occurs in the constant area of the supersonic ejector. For the mixed fluid to reach the sonic and sub-sonic condition, it is approximately x'= 11 for all cases.

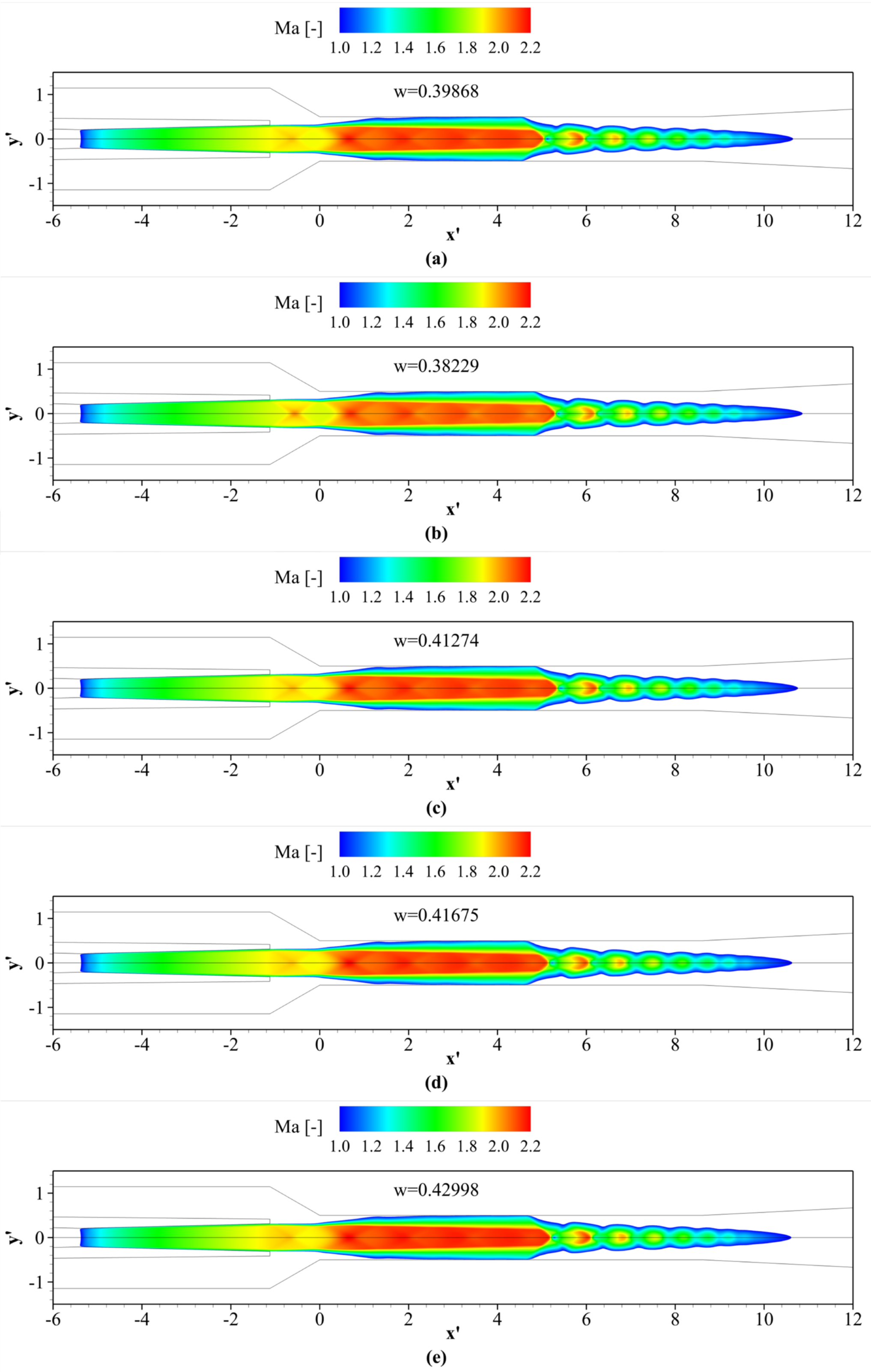

Figure 3.2 Mach Number Contours according to various refrigerants in the mixing section of the ejector; Case 1 (a), Case 2 (b), Case 2* (c), Case 3 (d) and Case 3* (e)

The series of oblique shocks in the supersonic ejector are illustrated by means of the shadowgraph technique for all cases using different refrigerants are used, as shown in Figure 3.3. The oblique shock series takes place in the mixing section of the supersonic ejector. First and second oblique shocks series occur in the vicinity of the inlet of the convergence duct and the exit of the constant area section of the mixing chamber, respectively. Meanwhile, the acceleration of the primary flow creates an annular cross-sectional area in the mixing chamber called the effective area. An increase in the expansion wave at the outlet of the primary nozzle results in a smaller annular area through which the secondary flow passes.

In this section of the thesis, results were obtained in terms of entrainment ratio (w) and flow structures using similar ejector geometry for the new generation R1234yf and R1234ze (E) refrigerants proposed as an alternative to R134a. In line with the obtained results, in the case of Case 2 using R1234yf fluid, lower entrainment ratio (w) was obtained compared to Case 1. However, as an alternative to this case, it was aimed to increase the entrainment ratio (w) by applying overheating at the primary and secondary fluid inlet for Case 2. Thus, in the case of Case 2* with overheating for R1234yf, better entrainment ratio (w) was obtained than Case 1 using R134a. On the other hand, Case 3 and Case 3* with overheating, using R1234ze (E), provided better entrainment ratio (w) value than Case 1. However, when the primary and secondary fluid obtained was evaluated in terms of mass flow rates, low values were obtained compared to Case 1.

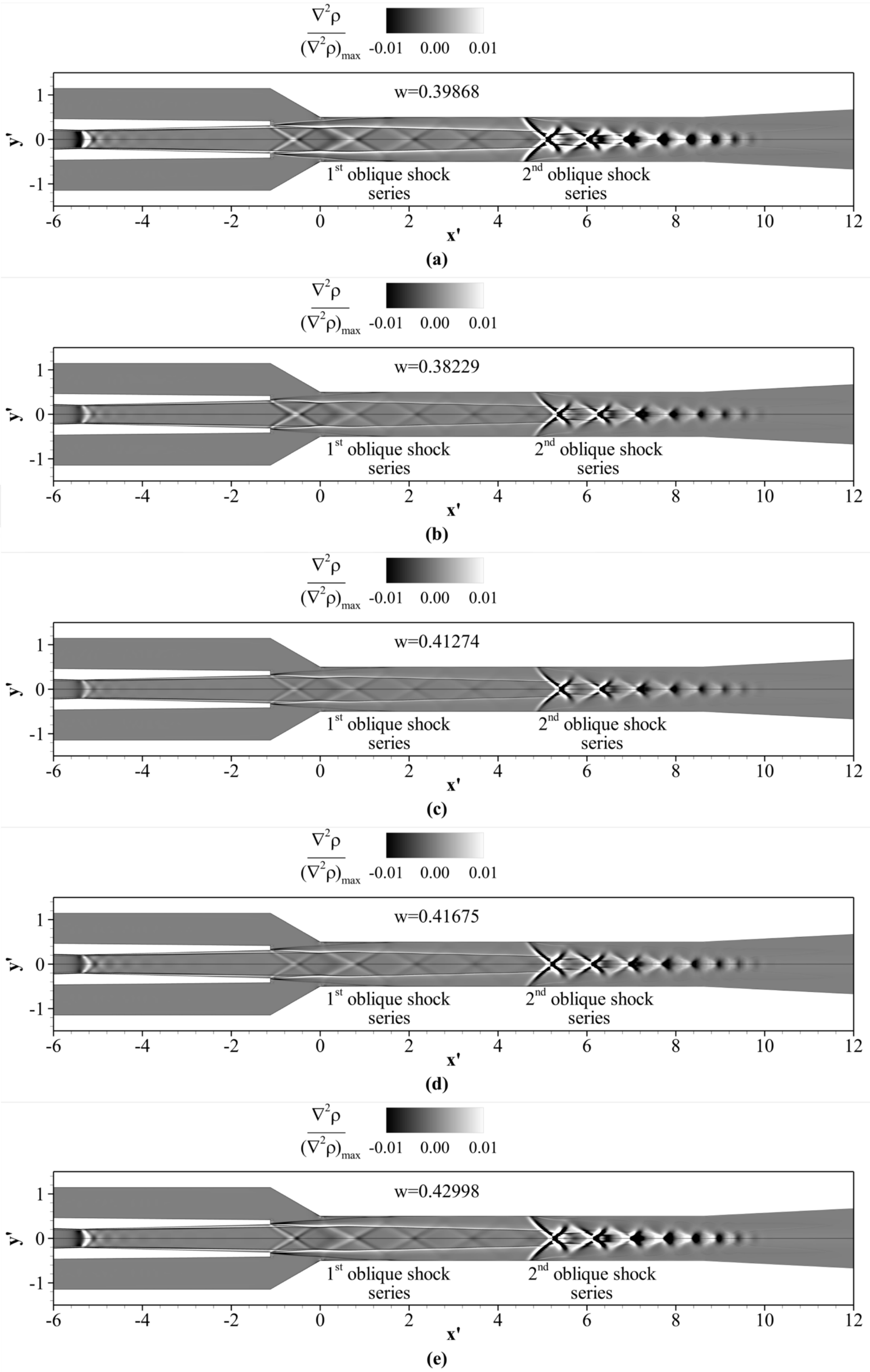

Figure 3.3 Interaction of the primary and secondary fluid flow in the mixing section of the ejector using shadowgraph technique for Case 1 (a), Case 2 (b), Case 2* (c), Case 3 (d), and Case 3* (e)

CHAPTER FOUR
INVESTIGATION OF EJECTOR PERFORMANCE FOR DESIGN PARAMETERS

The effects of primary nozzle position (*NXP*), the distance between the nozzle outlet and the inlet of the converging duct, and the converging duct angle of the mixing section (θ_{conv}) are investigated using R1234yf and R1234ze(E) instead of R134a through numerical simulations for the vapor-jet ejector in this section of the thesis. The effects of geometric parameters related to the ejector mixing section, entrainment ratio (*w*) variations, Mach number distributions along the symmetry axis, Mach number contours, and shadowgraphs are presented in detail for all different refrigerants.

4.1 Effect of the Primary Nozzle Exit Position

When the primary nozzle exit position (*NXP*) was investigated for different refrigerants, improvement to the entrainment ratio (*w*) value was observed due to the increase of *NXP*. In the previous section, the ejector geometry examined numerically using R134a was called Case 1. In this section, when the effect of the NXP parameter was examined, the suffix "a" has been added using similar names. It was aimed to compare the cases in which the best result was obtained in terms of the entrainment ratio (*w*). Accordingly, for the R1234a, R1234yf, R1234yf with overheating, R1234ze(E), and R1234ze(E) with overheating, the five different best entrainment ratio (*w*) values were named Case 1a, Case 2a, Case 2a*, Case 3a*, respectively. Depending on the primary nozzle exit position (*NXP*), the overall change in entrainment ratio (*w*) for different refrigerants was shown in Figure 4.1. For all cases, it was seen that the primary nozzle exit position (*NXP*), where the best entrainment ratio (*w*) was obtained, is approximately NXP'= -1.042.

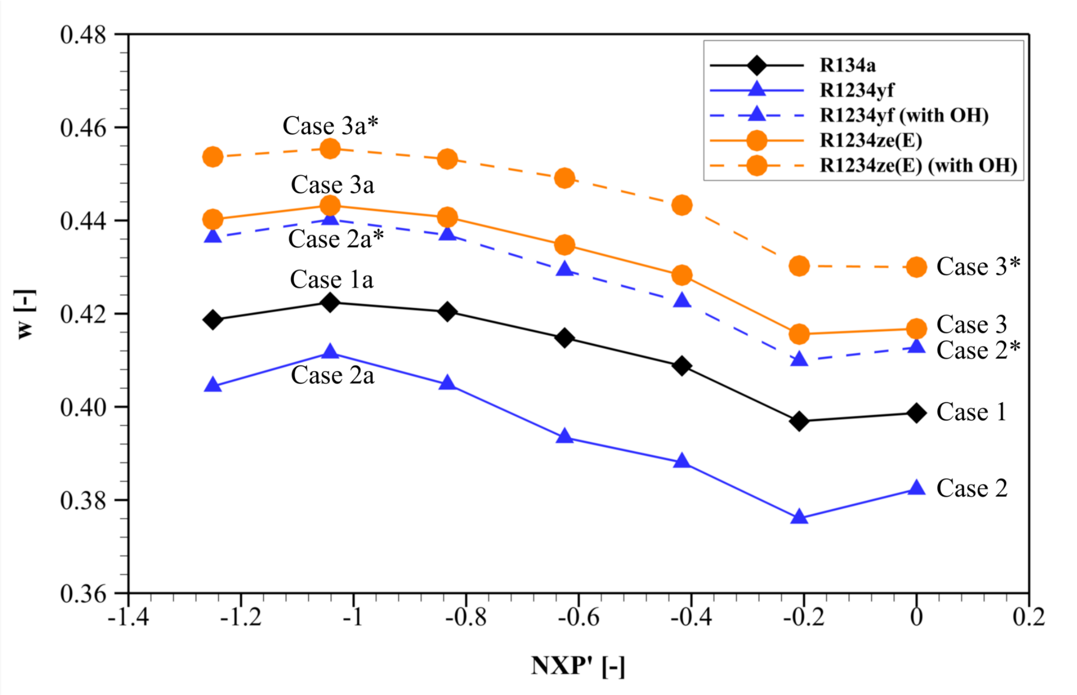

Figure 4.1 Effect of the primary nozzle exit position (*NXP*) of the ejector on the entrainment ratio (*w*)

In the results obtained, depending on the different primary nozzle exit position (*NXP*), the improvement rate for R134a (from Case 1 to Case 1a) was found at 5.95%. The improvement rate for R1234y used without overheating (from Case 2 to Case 2a) was 7.65%, and overheating was 6.65% (from Case 2* to Case 2a*). The improvement rate for R1234ze (E) (from Case 3 to Case 3a) was 6.35% and 5.92% for overheating (from Case 3* to Case 3a*). When the results in Figure 4.1 were generally evaluated, a decrease in performance was observed in terms of entrainment ratio (*w*) as a result of using R1234yf instead of R134 without overheating. This reveals that when using R1234yf fluid instead of R134a, similar performance should be achieved by making improvements in geometric and operating conditions. When R1234yf fluid is used with overheating, it is seen that a better performance is obtained in terms of entrainment ratio (*w*) than using R134a. On the other hand, when using R1234ze(E) instead of R134a, a better result is obtained in terms of entrainment ratio (*w*). In addition, in terms of performance increase due to *NXP* change, the best entrainment ratio (*w*) was achieved in the R1234ze(E) with overheating.

The cases where the best performance was obtained in terms of entrainment ratio (w) due to the primary nozzle exit position (*NXP*) change were obtained to compare Mach Number distribution along the x-axis, as shown in Figure 4.2. When the distribution of the Mach Number along the x-axis line is evaluated for all cases, it is seen that the secondary oblique shock series for Cases 1a, Case 3a, and Case3a* are in a similar position, approximately x'= 4.5. However, in cases of Case 2a and Case 2a*, secondary oblique shock series appears to occur approximately at the position of x'= 4.95. There is a similar difference in the mixing section of the ejector in returning to the subsonic condition. Case 1a, Case 3a and Case3a* return to the subsonic condition at approximately x'= 9.3, Case 2a and Case 2a* at approximately x'= 9.6.

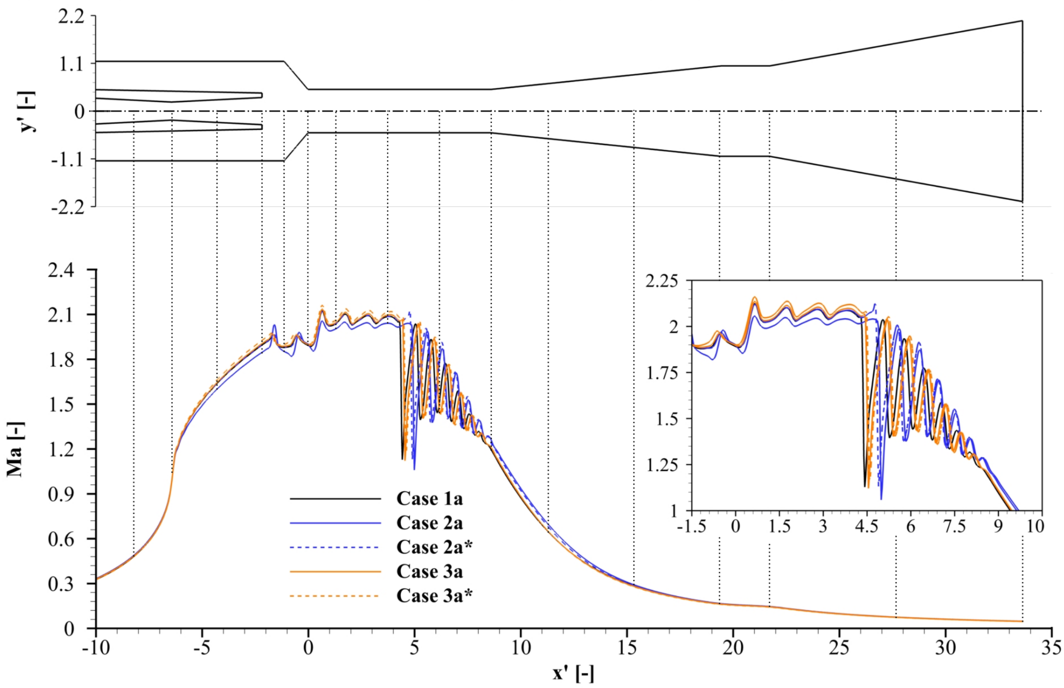

Figure 4.2 Mach Number distributions on the ejector symmetry axis for the primary nozzle exit position (*NXP*) which the best performance in terms of entrainment ratio (w) for different cases

In addition to the x-axis Mach number distribution, contour graphics were also provided for different cases. Contour plots for nozzle exit position (*NXP)* locations where the best entrainment ratio (w) was obtained for all cases are given in Figure 4.3. Through the contours of the Mach number, it is possible to have information about the structure of the flow that takes place in the ejector. When all the cases were compared, it can be seen that the primary fluid reaches sonic in the primary nozzle throat and supersonic conditions after its exit. Although primary and secondary shock series seen from Mach contours have similar structures, there are differences in shock position. Depending on the use of different fluids, although the operating conditions represent similar conditions, different values have been obtained as the entrainment ratio (*w*). The main reason for this difference is that the area called the effective area through which the secondary fluid can pass through the ejector is different in all cases.

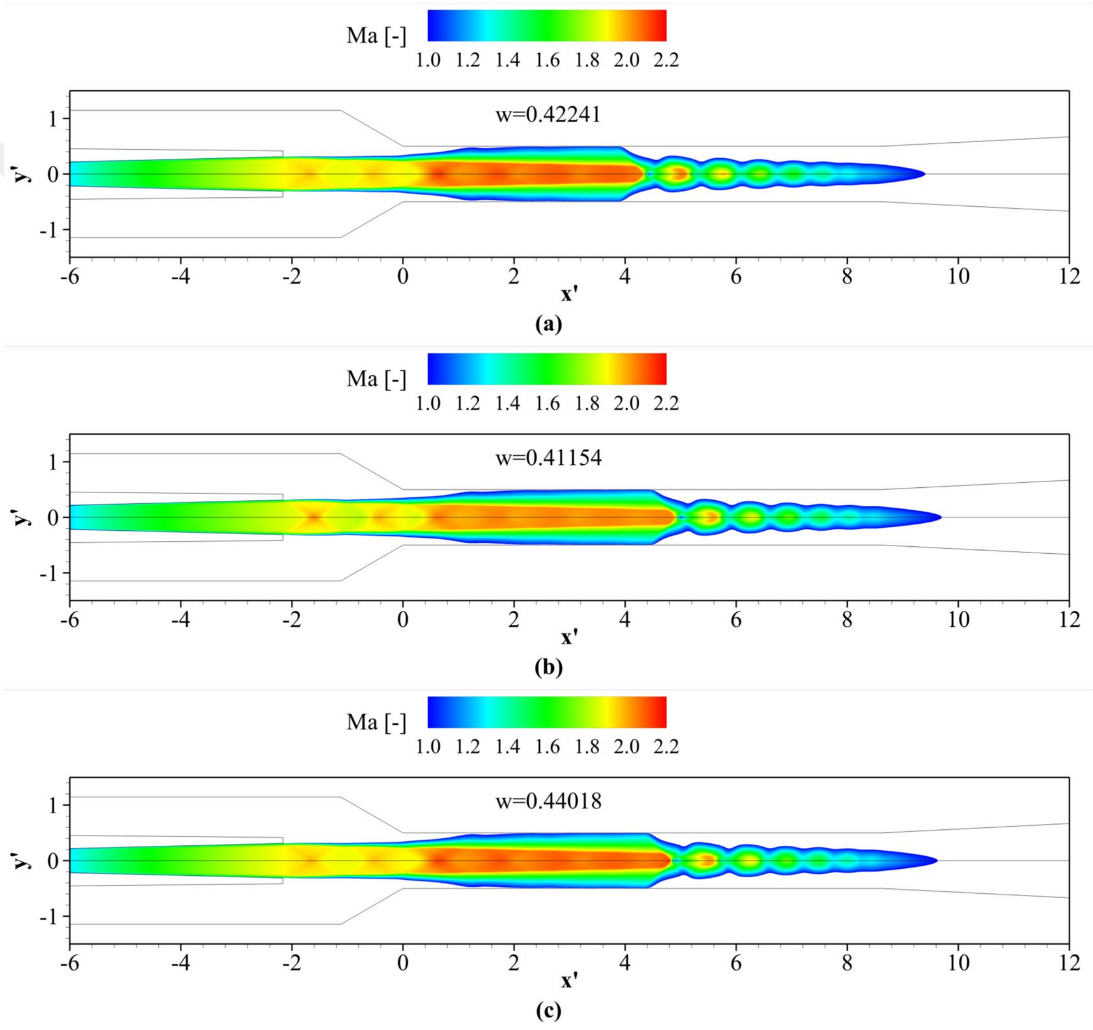

Figure 4.3 Mach Number Contours of the cases where the best performance was obtained in terms of the entrainment ratio (*w*) due to *NXP*; Case 1a (a), Case 2a (b), Case 2a* (c), Case 3a (d) and Case 3a* (e)

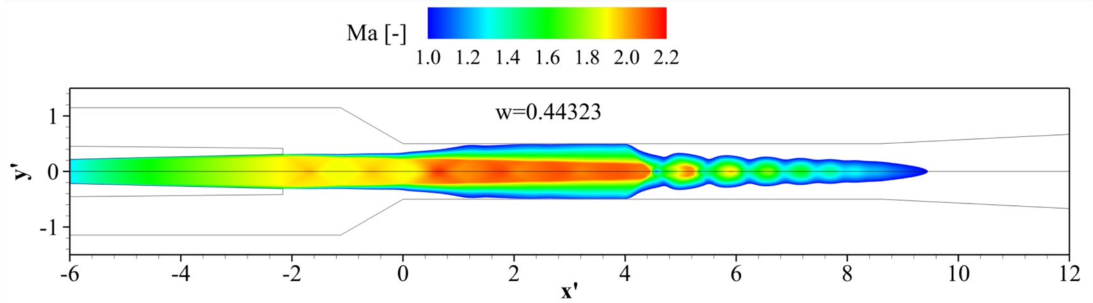

(d)

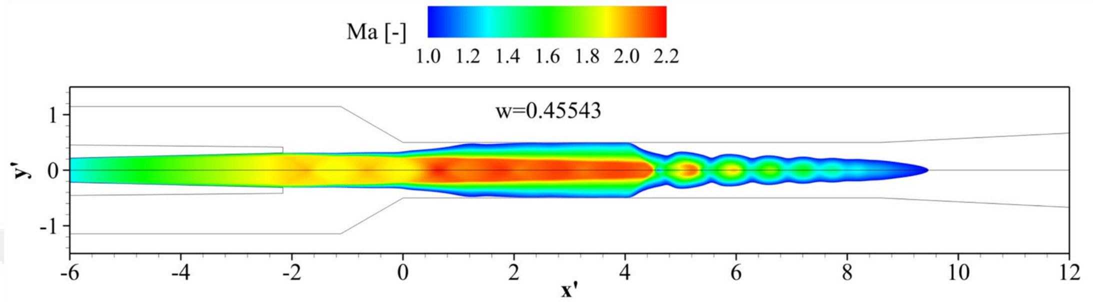

(e)

Figure 4.3 continues

The flow effect obtained when the primary nozzle was moved in the negative (-) x-direction in the ejector is directly understood from the shock series. The instantaneous density gradient, i.e., shadowgraph, within the flow area due to nozzle exit position (*NXP)* change, was presented for comparison in Figure 4.4. The variation of the shock series can be compared between the shadowgraphs of Case 1, Case 2, Case 2*, Case 3, and Case 3* discussed in Chapter 3 – Figure 3.3, the previous chapter, and the shadowgraphs in Figure 4.4.

When the flow structures due to the *NXP* change made through the geometry of the base cases (Case 1, Case 2, Case 2*, Case 3 and Case 3*), it is seen that the flow expansion angle after the primary nozzle outlet is lower compared to the base cases. Besides, the effect of the shock series in the mixing section of the ejector appears to be reduced. In other words, the motive jet flow that entrains the secondary fluid loses its flow power. However, with the movement of the primary nozzle in the negative x-direction, the area through which the secondary fluid can pass increases in the effect of change in *NXP*. Thus, an increase is provided in terms of entrainment ratio (*w*).

Motive jet flow loses power, while more secondary fluid entrained indicates an optimum value for *NXP* replacement. This situation was seen in Figure 4.1 when *NXP'*= -1.25 and *NXP'*= -1.042 positions are compared. When the primary nozzle is moved in the negative (-) x-direction from the *NXP* position, i.e., *NXP'*= -1.042, where the best entrainment ratio (w) was obtained, it was seen that the entrainment ratio (w) decreases. This shows that the motive jet flow, which has become even more weak, has weakened power to entrain the secondary fluid. For this reason, it is seen that each parameter forming an ejector geometry should be in the optimum value range.

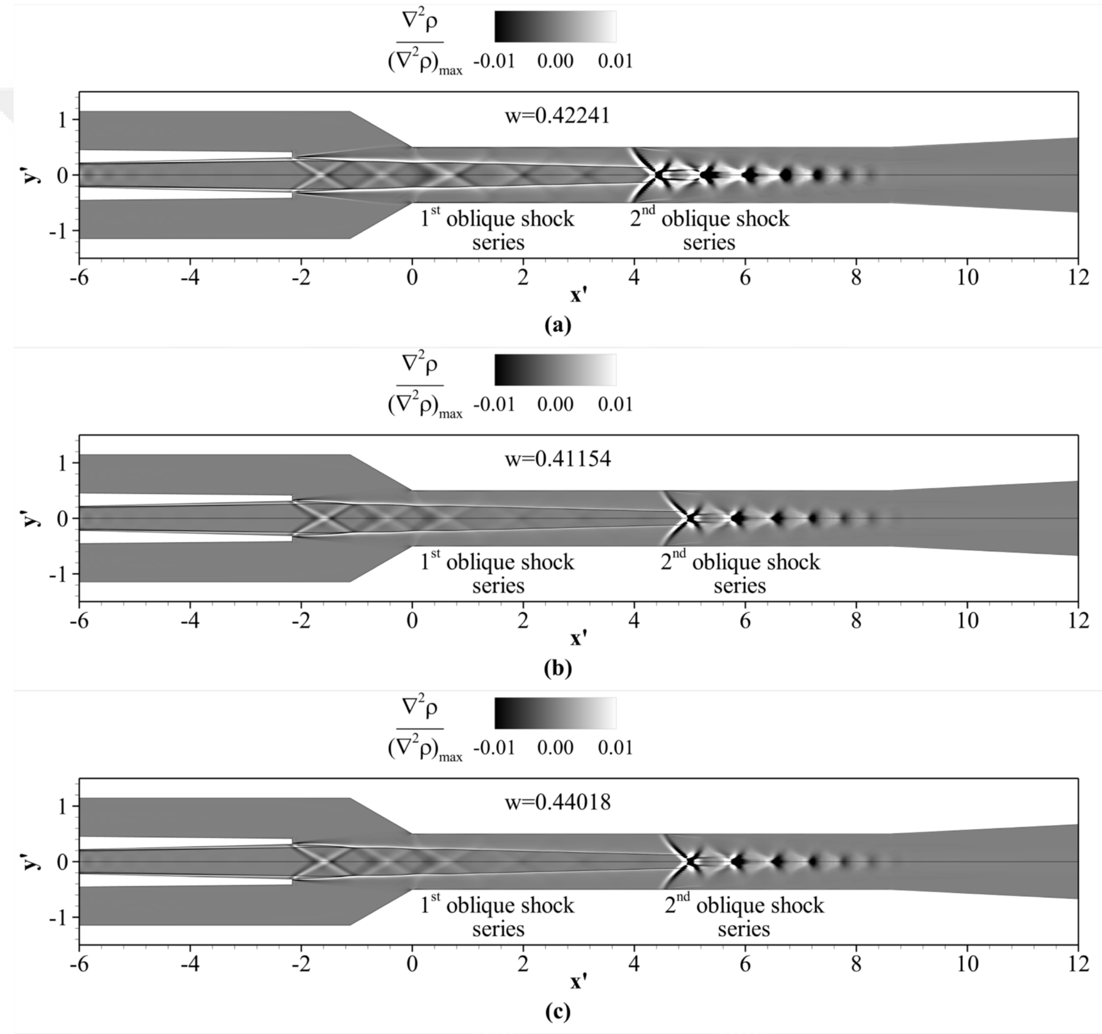

Figure 4.4 The interaction of primary and secondary fluid in case of the best performance in terms of entrainment ratio (w) due to *NXP*. Flow details in the mixing section of the ejector using the shadowgraph technique for Case 1a (a), Case 2a (b), Case 2a* (c), Case 3a (d) and Case 3a* (e)

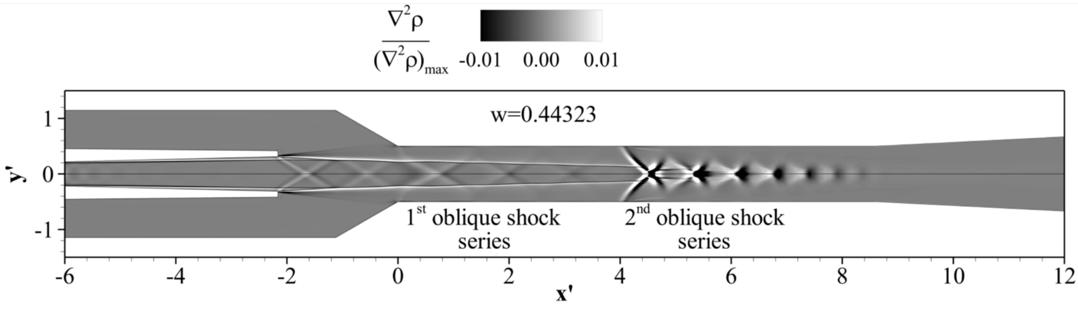

(d)

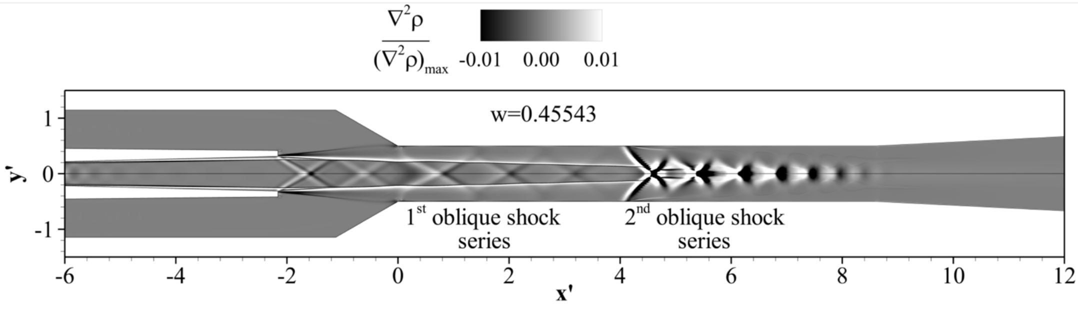

(e)

Figure 4.4 continues

4.2 Effect of the Converging Duct Angle of the Mixing Section

The entrainment ratio (w) of the vapor-jet ejector was obtained for approximately different fluids and operating conditions by changing the converging duct angle of the mixing section (θ_{conv}), as shown in Figure 4.5. It was aimed to compare the cases in which the best result is obtained entrainment ratio (w) depending on the converging duct angle of the mixing section (θ_{conv}). In this section, when the effect of the converging duct angle of the mixing section (θ_{conv}) was examined, the suffix "b" has been added using similar names. Accordingly, for the R1234a, R1234yf, R1234yf with overheating, R1234ze(E), and R1234ze(E) with overheating, the five different best entrainment ratio (w) values were named Case 1b, Case 2b, Case 2b*, Case 3b*, respectively.

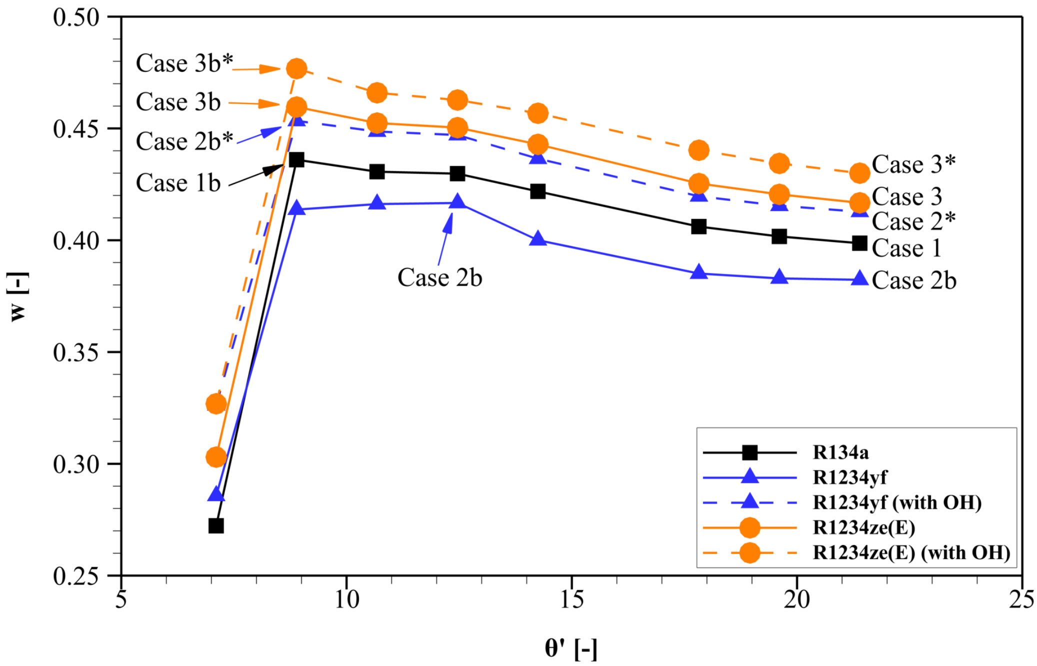

Figure 4.5 Effect of the converging duct angle (θ') of the ejector on the entrainment ratio (w)

It was considering all cases; the entrainment ratio (w) increases due to the decreasing converging duct angle of the mixing section. However, for values higher than a specific angle value, there is an instantaneous drop in entrainment ratio (w), and the ejector becomes unusable. The reason for this is that the primary nozzle cannot create the pressure difference required to accelerate the secondary fluid in the ejector. Therefore, the on-design and off-design conditions of the ejector should be considered within certain limits of the geometric improvements made in this way. In terms of entrainment ratio (w) for R134a (from Case 1 to Case 1b), the best improvement rate was found to be 9.36% due to the converging duct angle of the mixing section. The improvement rate for R1234yf used without overheating (from Case 2 to Case 2b) was 8.99%, and overheating was 9.85% (from Case 2* to Case 2b*). The improvement rate for R1234ze (E) (from Case 3 to Case 3b) was 10.28% and 10.88% for overheating (from Case 3* to Case 3b*).

Another conclusion that should be evaluated in Figure 4.5, Case 2b differs from the converging duct angle that gives the best entrainment ratio (w) compared to other cases. In all other cases except Case 2b, the best entrainment ratio (w) was obtained at

θ'=8.89, whereas for Case 2b θ'=12.46. The main reason for this situation is; even if the same ejector geometry is used first, it shows that it exhibits different ejector performance behaviors for different refrigerants and operating conditions. In other words, any change in the parameters of the ejector geometry changes the on-design and off-design performance curves of the ejector. Therefore, when it was aimed to increase the performance of the ejector geometry with geometric changes, a detailed optimization study should be carried out. The difference in terms of the entrainment ratio (w) between θ'= 8.89, where other cases indicate, and θ'=12.46, as stated by Case 2b, is approximately 0.71%. This difference indicates an almost linear deviation. Accordingly, there is this situation related to the increase in drag rate due to the decrease of the converging duct angle of the mixture section (θ_{conv}) modified on the basic ejector geometry. In terms of the entrainment ratio (w), the value was obtained in accordance with the converging duct angle range (Change of θ' value between 8.89 and 12.46) in which the best was obtained.

As shown in Figure 4.6, the Mach number distribution along the x-axis line of the ejector was described for different cases. The convergence angle of the mixing section (θ_{conv}) affects the flow structure in the mixing section of the ejector more than the primary nozzle exit position (*NXP*). This situation was seen when different shock positions were examined for the cases presented in Figure 4.6. When the Mach number distribution along the x-axis line was examined for all cases except Case 2b*, the first oblique shock series has a similar position. Nevertheless, the position of the second series of oblique shocks is different. The x' positions, where the second shock series was seen for Case 1b, Case 2b*, Case 3b, and Case 3b*, are approximately 2.5, 2.9, 3.2, and 3.8, respectively. When investigating only Case 2b, the Mach Number distribution shows significant differences along the x-axis line since it has a different converging duct angle of the mixing section (θ_{conv}) compared to other cases. For Case 2b, although it is similar to other cases except for the start position of the first shock series, the main difference is the start and end of the secondary shock series. The x' position of the start and end of the second shock series is approximately 5.5 and 9.2, respectively.

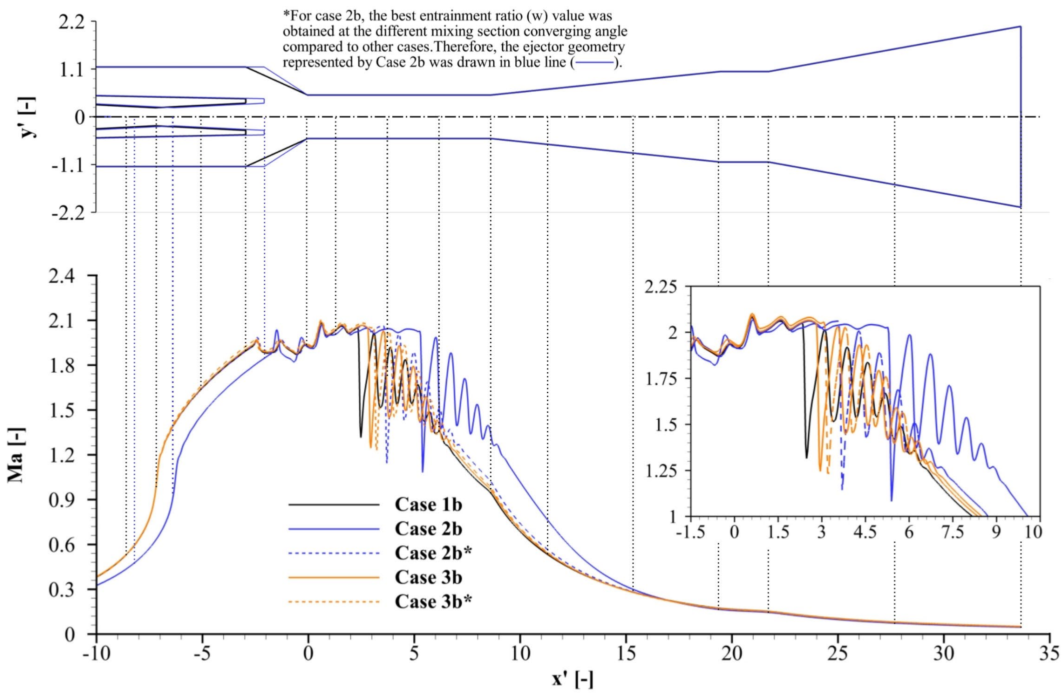

Figure 4.6 Mach Number distributions on the ejector symmetry axis for the converging duct angle of the mixing section (θ_{conv}), which the best performance in terms of entrainment ratio (*w*) for different cases.

The effect of the converging duct angle of the mixing section (θ_{conv}) was compared with the Mach number contours in which the entrainment ratio (*w*) obtained using different refrigerants, and operating conditions were obtained in Figure 4.7. In the results, It was seen that the change in the power of the propellant, the position where the flow reaches the supersonic state, and the intensity of the shock series was different. Case 1b using R134a has a weaker motive jet flow than other cases, and Case 1 (base case for R134a). Although it has a weaker motive jet flow, especially compared to Case 1, Case 1b flow has performed better as the entrainment ratio (*w*). This situation also applies to Case 2b, Case 2b*, Case 3b, and Case 3b*. In other words, it was concluded that, as the converging duct angle of the mixture section increases compared to the base geometry, there was better ejector performance in terms of the entrainment ratio (*w*), although there was a weak motive jet flow.

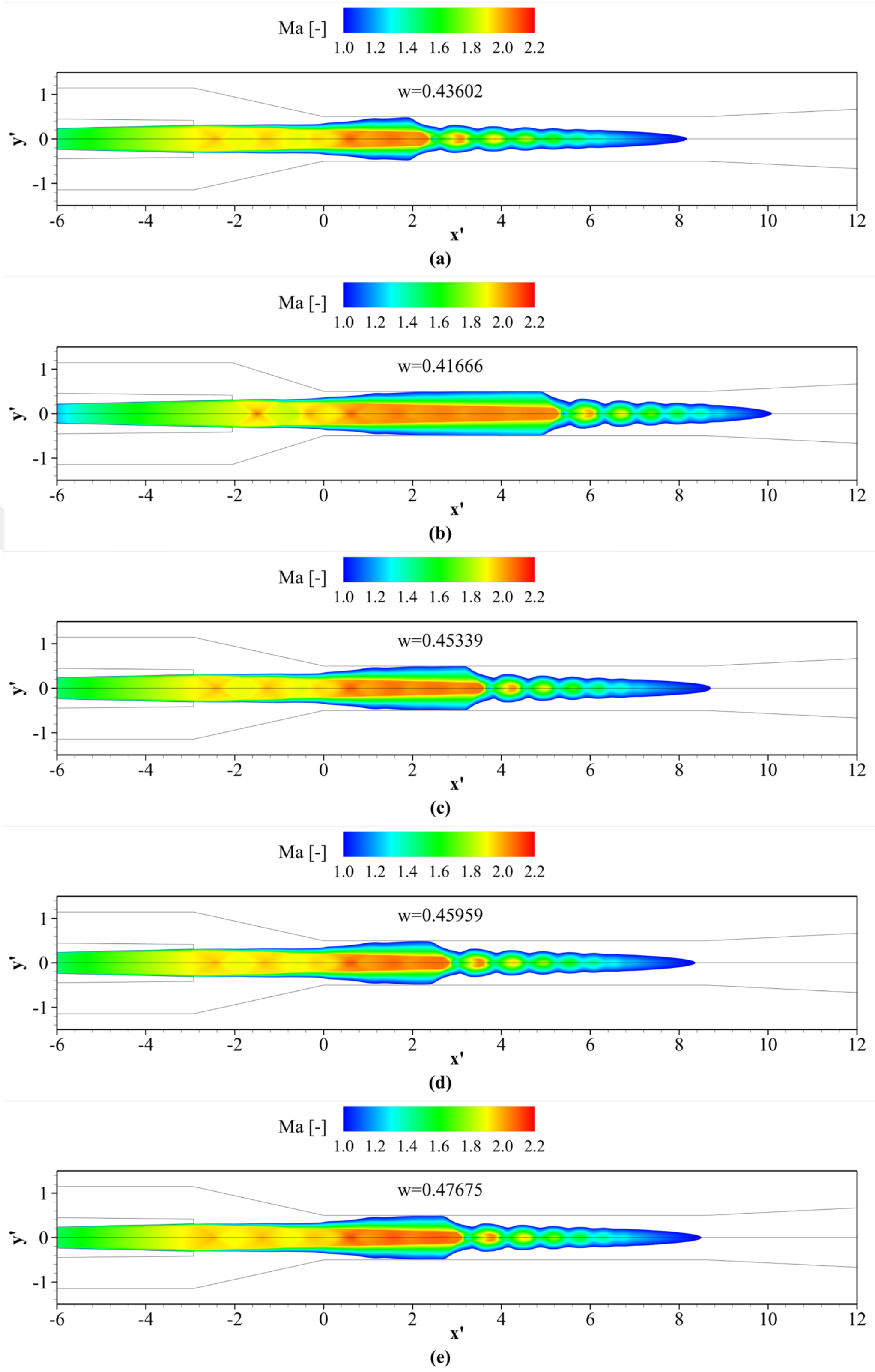

Figure 4.7 Mach Number Contours of the cases where the best performance was obtained in terms of the entrainment ratio (w) due to $\theta_{conv.}$; Case 1b (a), Case 2b (b), Case 2b* (c), Case 3b (d) and Case 3b* (e)

In addition to the x-axis Mach Number distribution and the Mach number contours c, the shadowgraph was presented for comparison in Figure 4.8 to see the particularly shock effects created by the converging duct angle of the mixing section (θ_{conv}) inside the mixing section of the ejector. Firstly, when Case 2b, which has a different converging duct angle of the mixing section (θ_{conv}) than other cases, was examined, it was seen that the effect of the primary shock series is the longest. Also, it appears that the secondary shock series affects the diffuser of the ejector. When the cases other than Case 2b are compared among themselves, it is seen that the primary shock series was in Case 2b*, which is the strongest.

When the best performance was obtained in terms of the entrainment ratio (w) as a result of changing the converging duct angle of the mixing section, it is important to compare it with the basic conditions in terms of performance evaluation. Shadowgraph was used to analyze this situation in terms of shock series. In this section, the best cases achieved in terms of the entrainment ratio (w) were compared to the base cases in Chapter 3 – Figure 3.3 and the shadow chart where the weaker motive jet was formed.

The increase in the entrainment ratio (w) as the converging duct angle of the mixing section (θ_{conv}) decreasing leads to an increase in the effective area required for the secondary fluid to pass when the less powerful motive jet was formed. However, as in the primary nozzle exit position (NXP), the other parameter of the ejector investigated, the converging duct angle of the mixing section (θ_{conv}) must be at an optimum value. For all cases, it was concluded that at converging duct angle of the mixing section (θ_{conv}) values lower than θ'=8.89, it is in an unusable off-design condition unless other fundamental dimensions or operating conditions of the referenced ejector were changed. Because the primary fluid of the ejector, motive jet fluid, becomes too weak to entrain the secondary fluid.

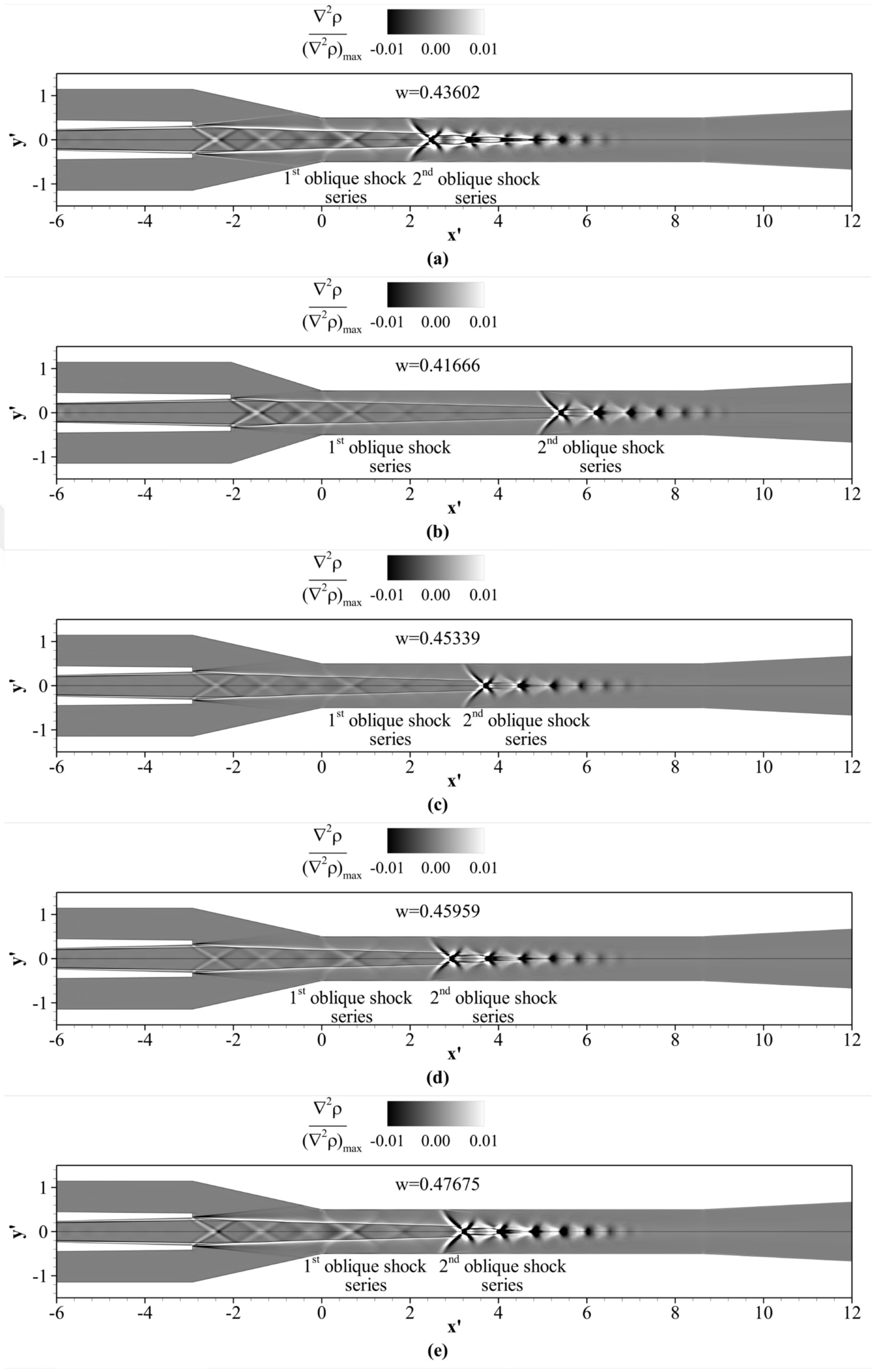

Figure 4.8 The interaction of primary and secondary fluid in case of the best performance in terms of entrainment ratio (w) due to θ_{conv}. Flow details in the mixing section of the ejector using the shadowgraph technique for Case 1b (a), Case 2b (b), Case 2b* (c), Case 3b (d) and Case 3b* (e)

CHAPTER FIVE
CONCLUSIONS

In this study, the performance evaluation for the ejector geometry, which is taken as reference from the literature, was made CFD model for the converging duct angle of the mixing section (θ_{conv}) and primary nozzle exit position (*NXP*) selected from the basic geometric parameters of the ejector. On the other hand, the effect of using R1234yf and R123ze(E) instead of R134a used in the reference study was investigated. The results are presented using the Mach number distribution along the x-axis, Mach Number contours, and shadowgraphs of the ejector. When the obtained values and graphs are evaluated for specified cases in general, the results can be summarized as follows:

- It was using R1234yf instead of R134a fluid: When using R1234yf, which is one of the new-generation environmentally friendly HFO refrigerants instead of R134a, which is in the process of being out of use, decreasing in ejector performance about 4.11% has been observed in terms of entrainment ratio (*w*) for similar operating conditions. Despite this situation, when R1234yf with 10°C overheating applied at the primary and secondary inlet of the ejector was used, 3.52% of the entrainment ratio (*w*) increasing was achieved. In line with the decrease and increase of ejector performance, it is very important to perform an optimization study in terms of geometric and working conditions in order to obtain higher performance when using R1234yf fluid instead of R134a.

- Using R1234yf instead of R134a fluid: When using R1234ze(E), another of the new generation environmentally friendly HFO refrigerants instead of R134a, 4.53% increase in ejector performance was observed in terms of the entrainment ratio (*w*) for similar operating conditions. Besides, ejector performance in terms of the entrainment ratio (*w*) was increased by 7.85% with 10°C overheating applied to the primary and secondary inlet. However, when R1234ze(E) was used under similar conditions instead of R134a, there was 23.71% reduction in the primary and secondary mass flow rates of the ejector. For the overheating situation, decrease of 26.72% was observed.

- Primary nozzle position (*NXP*): When the performance of the ejector was evaluated in terms of entrainment ratio (*w*), it was concluded that it could be increased by changing the primary nozzle exit position (*NXP*) for R134a, R1234yf, and R1234ze(E). The entrainment ratio (*w*) increase obtained for the R134a fluid was 5.95%, the performance increase obtained as a result of the primary nozzle exit position (*NXP*) change was 7.65% in the analyzes carried out using R1234yf instead of the R134a fluid and was obtained as 6.65% with overheating. When using R1234ze(E) instead of R134a, the increasing the entrainment ratio (*w*) obtained according to the primary nozzle exit position (*NXP*) change was calculated as 6.35% and 5.92% for the overheating.

- Converging duct angle of the mixing section (θ_{conv}): First of all, for all cases examined, it was concluded that the effect of the converging angle of the mixing section (θ_{conv}) on the entrainment ratio is a more effective parameter than primary nozzle exit position (*NXP*). Accordingly, In terms of the entrainment ratio (*w*) increase, the results were 9.36% for R134a. Also, It was calculated as 8.99% for R1234yf and 9.85% for R1234yf with overheating. When using R1234ze(E), the entrainment ratio (*w*) increase was calculated at 10.3%, and 10.9% for overheating.

In light of all this information, it is concluded that when the refrigerant is changed, the performance can be increased depending on the geometrical parameters and operating conditions. In the investigation of geometric and operating conditions using different refrigerants, detailed information could be obtained about the flow structures inside the ejector by using numerical models.

In line with the investigation of the ejector performance obtained for different cases, it was planned to be used in future studies, in the study of other geometric parameters of the ejector through the numerical model created in this thesis study. Besides, it was aimed to investigate the effect of ejector performance results obtained in this thesis and subsequent studies on the general performance of the refrigeration cycle. Consequently, it would be more comprehensible to what extent ejector performance affects the refrigeration cycle used.

The following paper was published under this thesis:

- Metin, C., Gök, O., Atmaca, A. U., & Erek, A. (2019). Numerical investigation of the flow structures inside mixing section of the ejector. *Energy*, *166*, 1216-1228.

REFERENCES

Allouche, Y., Bouden, C., & Varga, S. (2014). A CFD analysis of the flow structure inside a steam ejector to identify the suitable experimental operating conditions for a solar-driven refrigeration system. *International Journal of Refrigeration*, *39*, 186-195.

ANSYS, (2016). Introduction to ANSYS Fluent – Module 07: Turbulence. *ANSYS Inc.*, 12 April 2016.

Arun, K. M., Tiwari, S., & Mani, A. (2017). Three-dimensional numerical investigations on rectangular cross-section ejector. *International Journal of Thermal Sciences*, *122*, 257-265.

Banasiak, K., Palacz, M., Hafner, A., Buliński, Z., Smołka, J., Nowak, A. J., & Fic, A. (2014). A CFD-based investigation of the energy performance of two-phase R744 ejectors to recover the expansion work in refrigeration systems: an irreversibility analysis. *International Journal of Refrigeration*, *40*, 328-337.

Besagni, G. (2019). Ejectors on the cutting edge: The past, the present and the perspective. *Energy*, *170*, 998-1003.

Besagni, G., & Inzoli, F. (2017). Computational fluid-dynamics modeling of supersonic ejectors: Screening of turbulence modeling approaches. *Applied Thermal Engineering*, *117*, 122-144.

Besagni, G., Mereu, R., & Inzoli, F. (2016). Ejector refrigeration: a comprehensive review. *Renewable and Sustainable Energy Reviews*, *53*, 373-407.

Celik, I. B., Ghia, U., Roache, P. J., & Freitas, C. J. (2008). Procedure for estimation and reporting of uncertainty due to discretization in CFD applications. *Journal of Fluids Engineering-Transactions of The American Society of Mechanical Engineers*, *130*(7), 1-4.

Chunnanond, K., & Aphornratana, S. (2004). Ejectors: applications in refrigeration technology. *Renewable and Sustainable Energy Reviews*, *8*(2), 129-155.

Croquer, S., Poncet, S., & Aidoun, Z. (2016). Turbulence modeling of a single-phase R134a supersonic ejector. Part 1: Numerical benchmark. *International Journal of Refrigeration*, *61*, 140-152.

Date, A. W. (2005). *Introduction to computational fluid dynamics*. Cambridge: Cambridge University Press.

Del Valle, J. G., Jabardo, J. S., Ruiz, F. C., & Alonso, J. S. J. (2014). An experimental investigation of a R-134a ejector refrigeration system. *International Journal of Refrigeration*, *46*, 105-113.

Eames, I. W., Ablwaifa, A. E., & Petrenko, V. (2007). Results of an experimental study of an advanced jet-pump refrigerator operating with R245fa. *Applied Thermal Engineering*, *27*(17-18), 2833-2840.

Elbel, S., & Hrnjak, P. (2008). Ejector refrigeration: An overview of historical and present developments with emphasis on air conditioning applications, 12th Int. In *Refrigeration and Air Conditioning Conference, West Lafayette, IN*, 884.

Fang, Y., Croquer, S., Poncet, S., Aidoun, Z., & Bartosiewicz, Y. (2017). Drop-in replacement in a R134 ejector refrigeration cycle by HFO refrigerants. *International Journal of Refrigeration*, *77*, 87-98.

Gay, N.H. (1931). *Refrigerating system*. US Patent 1,836,318.

Hemidi, A., Henry, F., Leclaire, S., Seynhaeve, J. M., & Bartosiewicz, Y. (2009). CFD analysis of a supersonic air ejector. Part I: Experimental validation of single-phase and two-phase operation. *Applied Thermal Engineering*, *29*(8-9), 1523-1531.

Karthick, S. K., Rao, S. M., Jagadeesh, G., & Reddy, K. P. J. (2016). Parametric experimental studies on mixing characteristics within a low area ratio rectangular supersonic gaseous ejector. *Physics of Fluids*, *28*(7), 076101.

Kornhauser, A. A. (1990). The use of an ejector as a refrigerant expander. *International Refrigeration and Air Conditioning Conference*, 82.

Kranakis, E. F. (1982). The French connection: Giffard's injector and the nature of heat. *Technology and Culture, 23*(1), 3-38.

Lamberts, O., Chatelain, P., & Bartosiewicz, Y. (2017). New methods for analyzing transport phenomena in supersonic ejectors. *International Journal of Heat and Fluid Flow*, *64*, 23-40.

Lamberts, O., Chatelain, P., & Bartosiewicz, Y. (2018). Numerical and experimental evidence of the Fabri-choking in a supersonic ejector. *International Journal of Heat and Fluid Flow*, *69*, 194-209.

Lawrence, N., & Elbel, S. (2014). Experimental investigation of a two-phase ejector cycle suitable for use with low-pressure refrigerants R134a and R1234yf. *International Journal of Refrigeration*, *38*, 310-322.

Leblanc, M. (1910). *U.S. Patent Number 977,659*. Washington, DC: U.S. Patent and Trademark Office.

Lemmon, E. W., Huber, M. L., & McLinden, M. O. (2013). NIST standard reference database 23: reference fluid thermodynamic and transport properties-REFPROP, version 9.1, standard reference data program. *National Institute of Standards and Technology: Gaithersburg, MD*.

Li, D., & Groll, E. A. (2005). Transcritical CO2 refrigeration cycle with ejector-expansion device. *International Journal of refrigeration*, *28*(5), 766-773.

Li, H., Cao, F., Bu, X., Wang, L., & Wang, X. (2014). Performance characteristics of R1234yf ejector-expansion refrigeration cycle. *Applied Energy*, *121*, 96-103.

Little, A. B., Bartosiewicz, Y., & Garimella, S. (2015). Visualization and validation of ejector flow field with computational and first-principles analysis. *Journal of Fluids Engineering*, *137*(5), 051107.

Little, A. B., & Garimella, S. (2016a). A critical review linking ejector flow phenomena with component-and system-level performance. *International Journal of Refrigeration*, *70*, 243-268.

Little, A. B., & Garimella, S. (2016b). Shadowgraph visualization of condensing R134a flow through ejectors. *International Journal of Refrigeration*, *68*, 118-129.

Mazzelli, F., & Milazzo, A. (2015). Performance analysis of a supersonic ejector cycle working with R245fa. *International Journal of Refrigeration*, *49*, 79-92.

Metin, C., Gök, O., Atmaca, A. U., & Erek, A. (2019). Numerical investigation of the flow structures inside mixing section of the ejector. *Energy*, *166*, 1216-1228.

Mohamed, S., Shatilla, Y., & Zhang, T. (2019). CFD-based design and simulation of hydrocarbon ejector for cooling. *Energy*, *167*, 346-358.

Navarro-Esbrí, J., Moles, F., & Barragán-Cervera, Á. (2013). Experimental analysis of the internal heat exchanger influence on a vapour compression system performance working with R1234yf as a drop-in replacement for R134a. *Applied Thermal Engineering*, *59*(1-2), 153-161.

Omidvar, A., Ghazikhani, M., & Razavi, S. M. R. M. (2016). Entropy analysis of a solar-driven variable geometry ejector using computational fluid dynamics. *Energy Conversion and Management*, *119*, 435-443.

Özgür, A. E., Kabul, A., & Kizilkan, Ö. (2014). Exergy analysis of refrigeration systems using an alternative refrigerant (hfo-1234yf) to R-134a. *International Journal of Low-Carbon Technologies*, *9*(1), 56-62.

Regulation, E.U. (2014). No 517/2014 of the European Parliament and of the Council of 16 April 2014 on fluorinated greenhouse gases and repealing Regulation (EC) No 842/2006. *Official Journal of the European Union, 57*, 195-230.

Riffat, S. B., Gan, G., & Smith, S. (1996). Computational fluid dynamics applied to ejector heat pumps. *Applied Thermal Engineering*, *16*(4), 291-297.

Ruangtrakoon, N., Thongtip, T., Aphornratana, S., & Sriveerakul, T. (2013). CFD simulation on the effect of primary nozzle geometries for a steam ejector in refrigeration cycle. *International Journal of Thermal Sciences*, *63*, 133-145.

Rusly, E., Aye, L., Charters, W. W. S., & Ooi, A. (2005). CFD analysis of ejector in a combined ejector cooling system. *International Journal of Refrigeration*, *28*(7), 1092-1101.

Scott, D., Aidoun, Z., Bellache, O., & Ouzzane, M. (2008). CFD simulations of a supersonic ejector for use in refrigeration applications. *International Refrigeration and Air Conditioning Conference*, 927.

Sierra-Pallares, J., Del Valle, J. G., Carrascal, P. G., & Ruiz, F. C. (2016). A computational study about the types of entropy generation in three different R134a ejector mixing chambers. *International Journal of Refrigeration*, *63*, 199-213.

Sierra-Pallares, J., del Valle, J. G., Paniagua, J. M., García, J., Méndez-Bueno, C., & Castro, F. (2018). Shape optimization of a long-tapered R134a ejector mixing chamber. *Energy*, *165*, 422-438.

Sriveerakul, T., Aphornratana, S., & Chunnanond, K. (2007a). Performance prediction of steam ejector using computational fluid dynamics: Part 1. Validation of the CFD results. *International Journal of Thermal Sciences*, *46*(8), 812-822.

Sriveerakul, T., Aphornratana, S., & Chunnanond, K. (2007b). Performance prediction of steam ejector using computational fluid dynamics: Part 2. Flow structure of a steam ejector influenced by operating pressures and geometries. *International Journal of Thermal Sciences*, *46*(8), 823-833.

The Kigali Amendment to the Montreal Protocol: HFC Phase-down, UNEP, 28th meeting of Montreal Protocol, 10-14 October 2016, Kigali, Rwanda.

Union, E. (2006). Directive 2006/40/EC of the European Parliament and of the Council of 17 May 2006 relating to emissions from air-conditioning systems in motor vehicles and Amending Council Directive 70/156/EEC. *Official Journal of the European Union L*, *161*, 12-18.

Utomo, T., Ji, M., Kim, P., Jeong, H., & Chung, H. (2008). CFD analysis on the influence of converging duct angle on the steam ejector performance. *International Conference on Engineering Optimization, Rio de Janeiro, Brazil*. Retrieved July 06, 2020, from http://citeseerx.ist.psu.edu/viewdoc/download?doi=10.1.1.608.3326&rep=rep1&type=pdf.

Varga, S., Lebre, P. M., & Oliveira, A. C. (2013). CFD study of a variable area ratio ejector using R600a and R152a refrigerants. *International Journal of Refrigeration*, *36*(1), 157-165.

Varga, S., Oliveira, A. C., & Diaconu, B. (2009a). Influence of geometrical factors on steam ejector performance–a numerical assessment. *International Journal of Refrigeration*, *32*(7), 1694-1701.

Varga, S., Oliveira, A. C., & Diaconu, B. (2009b). Numerical assessment of steam ejector efficiencies using CFD. *International Journal of Refrigeration*, *32*(6), 1203-1211.

Varga, S., Soares, J., Lima, R., & Oliveira, A. C. (2017). On the selection of a turbulence model for the simulation of steam ejectors using CFD. *International Journal of Low-Carbon Technologies*, *12*(3), 233-243.

Wang, L., Yan, J., Wang, C., & Li, X. (2017). Numerical study on optimization of ejector primary nozzle geometries. *International Journal of Refrigeration*, *76*, 219-229.

Watanawanavet, S. (2005). *Optimization of a high-efficiency jet ejector by computational fluid dynamic software.* Phd Thesis, A&M University, Texas.

Wu, H., Liu, Z., Han, B., & Li, Y. (2014). Numerical investigation of the influences of mixing chamber geometries on steam ejector performance. *Desalination*, *353*, 15-20.

Wu, Y., Zhao, H., Zhang, C., Wang, L., & Han, J. (2018). Optimization analysis of structure parameters of steam ejector based on CFD and orthogonal test. *Energy*, *151*, 79-93.

Yapıcı, R., Ersoy, H. K., Aktoprakoğlu, A., Halkacı, H. S., & Yiğit, O. (2008). Experimental determination of the optimum performance of ejector refrigeration system depending on ejector area ratio. *International Journal of Refrigeration*, *31*(7), 1183-1189.

Zhu, Y., & Jiang, P. (2014). Experimental and numerical investigation of the effect of shock wave characteristics on the ejector performance. *International Journal of Refrigeration*, *40*, 31-42.

Zhu, Y., Cai, W., Wen, C., & Li, Y. (2009). Numerical investigation of geometry parameters for design of high performance ejectors. *Applied Thermal Engineering*, *29*(5-6), 898-905.

Zilio, C., Brown, J. S., Schiochet, G., & Cavallini, A. (2011). The refrigerant R1234yf in air conditioning systems. *Energy*, *36*(10), 6110-6120.

APPENDICES

APPENDIX-1: Nomenclature

A	Area [m^2]
D	Diameter [m]
E	Total energy [J]
e	Relative error [-]
h	Representative mesh size [-]
HDERC	Heat-driven ejector refrigeration cycle
EERC	Ejector expansion refrigeration cycle
k	Thermal conductivity [W/mK]
L	Length [m]
Ma	Mach number [-]
$\dot{m}$	Mass flow rate [kg/s]
N	Total cell number [-]
P	Pressure [Pa]
r	Refinement factor [-]
s	Sign function
T	Temperature [C]
V	Velocity [m/s]
w	Entrainment ratio [-]
x	Location on the x-coordinate [m]
x'	The ratio of x-coordinate to D_{const} [-]
y	Location on the y-coordinate [m]
y'	The ratio of y-coordinate to D_{const} [-]
NXP	Nozzle exit position [m]
NXP′	The ratio of NXP to D_{const} [-]
GCI	Grid convergence index [-]
OH	Overheating

Greek Letters

θ	Angle
θ'	The ratio of θ_{conv} to θ_p [-]
ρ	Density [kg/m^3]
τ	Stress tensor [N/m^2]
μ	Dynamic viscosity [Ns/m^2]
ε	The calculated value difference between grids
φ	Any variable selected in the flow field for GCI study
γ	Heat capacity ratio [-]
$\prod$	Compression ratio [-]
ξ	Expansion ratio [-]

Subscripts

conv	Converging duct of the ejector
const	Constant area mixing section of ejector
comp	Compression
throat	The throat of the primary nozzle
diff	Diffuser
exp	Expansion
in	Inlet
out	Outlet
i, j	Space components
eff	Effective
p	Primary (motive) fluid/nozzle
s	Secondary fluid
max	Maximum
Coarse	Coarse mesh structure
Medium	Medium mesh structure
Fine	Fine mesh structure
c	Critical